Project title: Scanning Radar Investigations to Characterize Cloud and Precipitation Processes for ASR
Project Final Report DOE Award No. DE-SC0008583

Publication list:

Journal Articles

1. Yoshikawa, E., V. Chandrasekar, T. Ushio, and T. Matsuda, 2016: A Bayesian Approach for Integrated Raindrop Size Distribution (DSD) Retrieval on an X-Band Dual-Polarization Radar Network. *J. Atmos. Oceanic Technol.,* **33**, 377–389, doi: 10.1175/JTECH-D-15-0060.1.
2. Eiichi Yoshikawa, V. Chandrasekar, and Tomoo Ushio, 2014: Raindrop Size Distribution (DSD) Retrieval for X-Band Dual-Polarization Radar. J. Atmos. Oceanic Technol., 31, 387–403.
3. Tyynela, J., and V. Chandrasekar, 2014: Characterizing falling snow using multifrequency dual-polarization measurements. Journal of Geophysical Research: Atmospheres, 119, 8268–8283.
4. Junyent, F. and V. Chandrasekar, 2016: An Examination of Precipitation Using CSU–CHILL Dual-Wavelength, Dual-Polarization Radar Observations. J. Atmos. Oceanic Technol., 33, 313–329.
5. C. R. Williams, R. M. Beauchamp and V. Chandrasekar, 2016: Vertical Air Motions and Raindrop Size Distributions Estimated Using Mean Doppler Velocity Difference From 3- and 35-GHz Vertically Pointing Radars. *IEEE Transactions on Geoscience and Remote Sensing*, 54(10), 6048-6060.
6. Vaccarono, M., Bechini, R., Chandrasekar, C. V., Cremonini, R., and Cassardo, C, 2016: An integrated approach to monitoring the calibration stability of operational dual-polarization radars, Atmos. Meas. Tech., 9, 5367-5383.

Conferences Publications: There are numerous conference papers, and for brevity citations for only a select few are listed.

Dmitri Moisseev, Larry Bliven, Pablo Saavedra, Susanna Lautaportti, Alessandro Battaglia, V. Chandrasekar , Inference of dominating snow growth processes from radar observations, The 7th European Conf. Radar Meteorology Hydrology (ERAD), Toulouse, France, June 25-29, 2012.

Joseph C Hardin, V. Chandrasekar, Eiichi Yoshikawa, Tomoo Ushio, "Integrated framework for retrievals in a networked radar environment: Application to the Mid-latitude Continental Convective Clouds Experiment," AGU (American Geophysical Union) Fall Meeting, San Francisco, CA, 3-7 December 2012.

V. Chandrasekar, Joseph C. Hardin and Michael P. Jensen, "Error characterization of retrievals for active remote Sensing instruments in the ARM climate research facility at the Southern Great Plains site", AGU (American Geophysical Union) Fall Meeting, San Francisco, CA, 3-7 December 2012.

Joseph C. Hardin and V. Chandrasekar, "Calibration of Ground Radars During the Mid Latitude Continental Convective Cloud Experiment (MC3E)", Proc. of 2013 USNC-URSI National Radio Science Meeting, Boulder, Colorado, USA, January 9-12, 2013.

Jani Tyynela and V. Chandrasekar, "Characterizing falling snow using multi-frequency dual-polarization measurements", 36th Conference on Radar Meteorology, Breckenridge, USA, September 16-20, 2013.

Eiichi Yoshikawa, N. Matayoshi, T. Ushio, and V. Chandrasekar, "Integrated Velocity Retrieval on Radar Network Environment", 36th Conference on Radar Meteorology, Breckenridge, USA, September 16-20, 2013.

Dmitri Moisseev, V. Chandrasekar, Susanna Lautaportti, and Pablo Saavedra, 2014: Radar-Radiometer Synergistic Inference of Prevailing Snowflake Growth Mechanisms. Proceedings of the 13th Specialist Meeting on Microwave Radiometry and Remote Sensing of the Environment, Pasadena, California, 24-27 March 2014.

V. Chandrasekar, Cuong Nguyen, Nitin Bharadwaj, and Hans Verlinde, 2014: Simultaneous polarimetric X-band and Ka-band radar observations of clouds and mixed phase precipitation over the North Slope of Alaska. Proceedings of the 8th European Conf. on Radar in Meteorology and Hydrology (ERAD2014), Garmisch-Partenkirchen, Germany, 1-5 September 2014.

Ljubov Nevvonen, Dmitri Moisseev, V. Chandrasekar, and Heikki Pohjola, 2014: Dual-polarization based QPE in presence of hail contamination. Proceedings of the 8th European Conf. on Radar in Meteorology and Hydrology (ERAD2014), Garmisch-Partenkirchen, Germany, 1-5 September 2014.

Cuong Nguyen and V. Chandrasekar, 2014: An Improved Method for Detectingand Separating Cloud from Drizzle Radar Signatures Using a Time Domain Parametric Technique. Proceedings of AGU Fall Meeting, San Francisco, California, 15-19 December 2014.

Joseph Hardin and V. Chandrasekar, 2015: PyDisdrometer: A Python Library for Disdrometer Data Processing and Radar Simulation. Proceedings of the 95th AMS Annual Meeting, Phoenix, AZ, 04-08 January 2015.

Hardin, J. C., and V. Chandrasekar, 2015: A cross frequency performance comparison of dual polarization attenuation correction algorithms at X and S band. IGARSS2015, Munich, Germany.

V. Chandrasekar, Shashank Joshil, and Pratik Ramdasi, 2016: "Separation of Cloud and Drizzle Using Spectral Analysis for ARM Cloud Radar," Proc. 2016 USNC-URSI National Radio Science Meeting, Boulder, Colorado, USA, January 6-9, 2016.

Chandrasekar, V., Shashank S. Joshil, Pratik Ramdasi, 2016: Separation of cloud and drizzle using spectral Analysis for arm cloud radar. USNC URSI National Radio Science Meeting, Boulder, CO.

Contributions by research topics:

A. Development for Cloud drizzle separation studies for the ENA site based on Doppler Spectra.

Separation of cloud and drizzle microphysics and turbulence in warm clouds is extremely useful to shed light on precipitation initiation, including the role of aerosols and dynamics. Beyond the basic development of precipitation, the consequences of the in-cloud formation of drizzle and its sub-cloud evaporation are potentially critical determinants of cloud structural variation in the marine boundary layer, which impacts the development and maintenance of warm clouds and the corresponding radiative effects. This section prepares a robust data product just to address this problem from profiling cloud radars, using a robust mathematical technique developed by the PIs team termed PTDM (parametric time domain method). A journal article is being prepared based on this work. Doppler spectral analysis of radar observations have been pursued since the early days of radar meteorology. This has been used extensively in clear air and precipitation profilers extensively. Spectral analysis in the standard weather radars have also come a long way enabled by the rapid advancement in high speed signal processors. Precipitation profilers have significantly advanced the art of separating the various components within the vertical looking Doppler observation profiles (Gage, 1990, Gossard 1988, Moissev and Chandrasekar ,2007). More recently Luke and Kollias (2013) used spectral analysis techniques to separate cloud and precipitation components using vertical profile of Doppler Spectra. Spectral analysis is a very well developed topic in the study of signal processing and it spans multiple disciplines all the way from geosciences to engineering. In this context we propose an advanced signal processing technique developed by the PI group to study the cloud drizzle separation and parameter estimation using ARM vertically pointing cloud radars in conjunction with other instruments.

Radar signals can be represented as a sum of individual signals coming from scatters in the radar resolution volume. Because the individual signals have similar statistical properties, the joint probability density function of real and imaginary parts of the received signal can be considered to be zero mean normal (Bringi and Chandrasekar 2001). The multivariate probability density function of the complex voltage can be expressed through its joint distribution function (Bringi and Chandrasekar 2001).

The multivariate probability density function of the complex voltage can be written as:

$$f(V) = \frac{1}{\pi^N \det(R)} \exp(-V^H R^{-1} V)$$

$$= \frac{1}{\pi^N \det(R)} \exp(-trace(R^{-1} R_V)] \quad \text{... (A1)}$$

Where, V is the vector of the received signal samples, $R = E(VV^H)$ is the covariance matrix and $R_V = VV^H$ is the sample covariance matrix. Here, superscript H denotes the Hermitian. If different echo types are present within the same radar observation volume, then the observed Doppler Spectrum can be written as

$$S(v) = \sum_{i=1}^{N} S_i(v) + P_n \quad \text{... (A2)}$$

Where

$$S_i(v) = \frac{S_i(p)}{\sigma_i\sqrt{2\pi}} e^{-\frac{(v-\bar{v}_i)^2}{2\sigma_i^2}} \quad \text{..... (A3)}$$

We can use this model to make cloud particle spectrum and drizzle particle spectra as two different sets of radar echoes.

When we have just cloud and drizzle together N is 2. The spectral moments of the signals can be obtained by minimizing the negative log-likelihood as

$$L(\mu) = \ln(\det(\mathbf{R}(\mu))) + trace\left(\hat{\mathbf{R}}\mathbf{R}^{-1}(\mu)\right) \quad \text{(A4)}$$

Where

$$\mu = \left[\bar{v}_1, \sigma_1, P_1, ..., \bar{v}_N, \sigma_N, P_N, p_n\right]$$

The likelihood function in (7) can have several minima. To retrieve unknown parameters one needs to make sure that an optimization outcome of (7) converges to a global minimum. To achieve this, it is important to properly select seed values for the nonlinear optimization procedure.

Where R() and R are the sample covariance matrix and the model covariance matrix, respectively. When the signal only contains one type of echo, its Doppler power spectrum follows a Gaussian shape (N=1). However, in the present of drizzle and cloud mixture, the resulting spectral shape can depart from Gaussian. In such case, goodness of fit parameters could be used to detect the present of drizzle in the mixture which is described in the error structure of the procedure

The cloud drizzle separation algorithm is summarized as follows:

- First, the cloud, drizzle map (C/D map) is created using PTDM goodness of fit parameters. It is noted that PTDM is only applied to signals above Cloud base.

- The C/D map is processed (smoothened) to reduce the estimate uncertainty.
- Re-apply PTDM with two-echo model for the gates with the presence of drizzle.

Classify cloud and drizzle echoes in a way so that it remains the continuity of drizzle signals below and above the Cloud base. The architecture of the cloud drizzle separation is shown in Fig A1.

The advanced parametric modeling method works with a single radar power spectra profile and performs well in most scenarios. Drizzle reflectivity can be obtained accurately without the need of a compensation factor when cloud and drizzle echoes overlap heavily. The applications of the technique include inference of the vertical air motion, drizzle drop size distribution, and the dynamical and microphysical processes during the transition from cloud to drizzle.

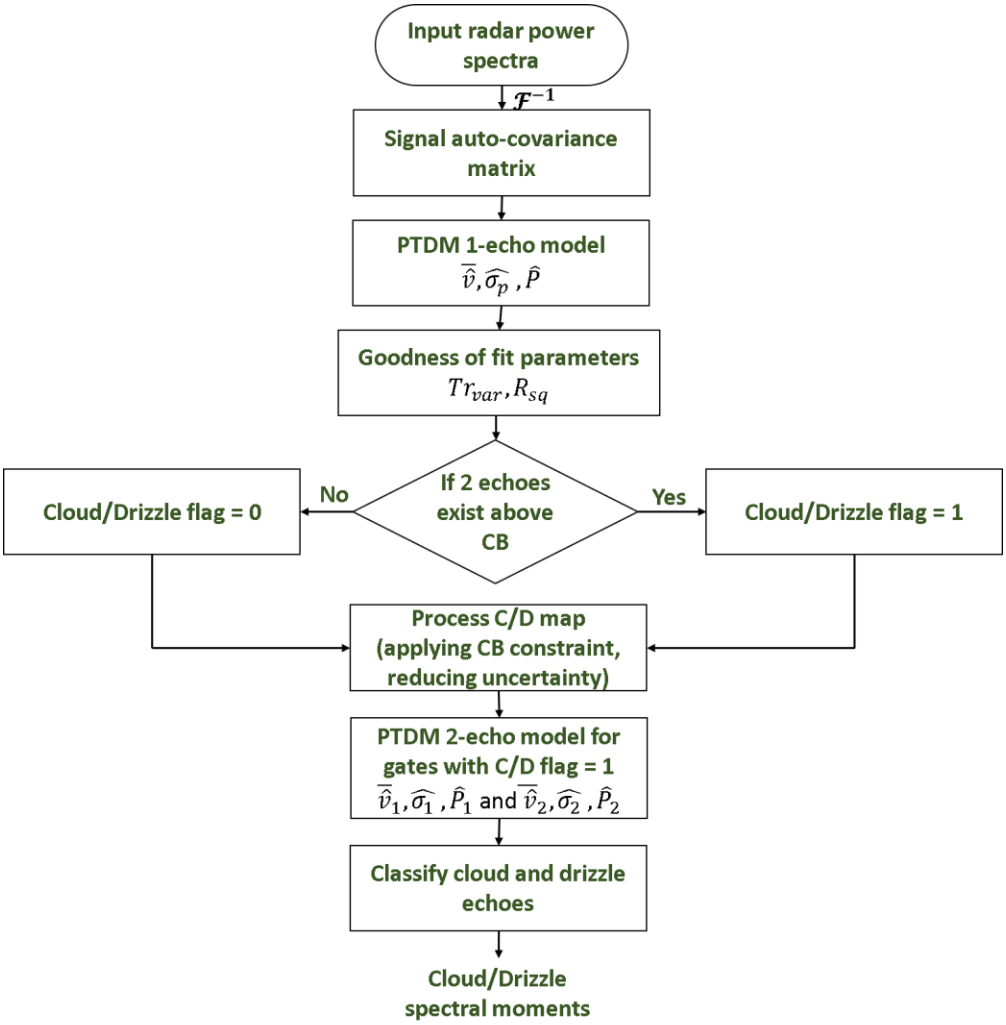

Figure A1. The Architecture of the Cloud Drizzle separation System.

Fig A2 shows an example retrieval of cloud drizzle separation from ARM cloud radar. The figure on the left shows the time resolved vertical profile of reflectivity and velocity whereas the figure in the middle shows the cloud profiles and the figure on the right shows the drizzle profiles. These profiles are directly from the code, and no corrections have been made that shows the robustness of the procedure.

The following Fig A2 shows the cloud drizzle separation methodology for one spectrogram. This can be implemented and extended over time to get full scale retrieval. This technique is a further expansion and refinement of the spectra based technique developed by Luke et al (2013). Subsequently the observations can be developed into a cloud drizzle separation product as shown in Fig A3.

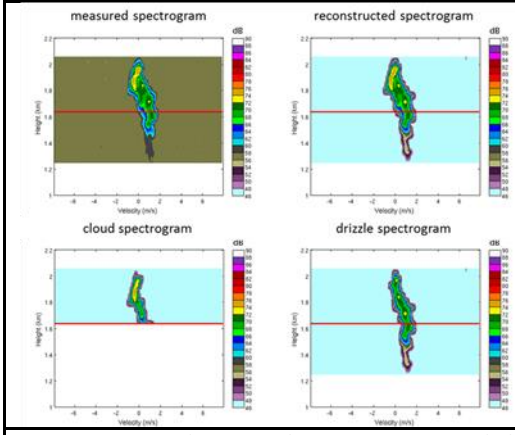

Figure A2. Radar Doppler spectrum and the spectral separation

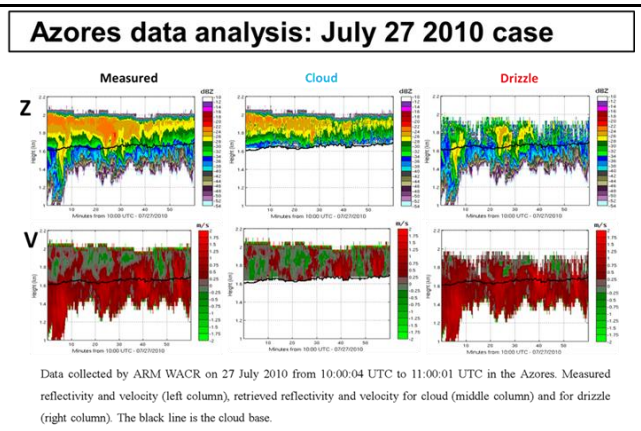

Figure A3. Time profile of cloud drizzle separation

B. Advanced radar retrieval for the SGP site.

This research essentially focused on microphysical retrievals to get the retrievals from both X band radars and networked observations in SGP. A raindrop size distribution (DSD) retrieval method for a weather radar network consisting of several X-band dual-polarization radars is proposed. An iterative maximum likelihood (ML) estimator for DSD retrieval in a single radar was developed in our previous work, and the proposed algorithm in this paper extends the single radar retrieval to radar networked retrieval, where ML solutions in each single radar node are integrated based on a Bayesian scheme in order to reduce estimation errors and enhance accuracy. Statistical evaluations of the proposed algorithm were carried out using radar simulations. The results with eight radar nodes showed that bias and standard errors are - 0.05 and 0.09 in log(Nw); Nw (mm-1m-3 33) and 0.04 and 0.09 in D0 (mm) in an environment with fluctuations in dual-polarization radar measurements (normal distributions with standard deviations of 0.8 dBZ, 0.2 dB, and 1.5 deg in Zhm, Zdrm, and ΦDPm, respectively). Further error analyses indicated that estimation accuracy depended on the number of radar nodes, ranges of varying μ, raindrop axis ratio model, and system bias errors in dual-polarization radar measurements. These results have been reported in multiple articles.

The SGP site is a unique site and has a network of X-band radars and a C-band radar (in addition to K and W band systems). The PI specialized in developing networked radar retrieval algorithms, which have

resulted that have been published in peer-reviewed literature. Single radar algorithms were also published in peer-reviewed literature.

B.1. Methodology

B.1.1. Background

The three dual-polarization measurements of measured reflectivity—horizontal polarization, ZHm; measured differential reflectivity, ZDRm; and measured differential propagation phase, ΦDPm—are the inputs of the NTR. Strictly speaking, these three measurements are input to the SRR, and then the results of the SRR are input to the NTR. In this subsection, the relations between the three dual-polarization measurements and the DSD are described as follows:

$$Z_{\mathrm{Hm}}(r) = Z_H(r) - 2\times 10^{-3}\int_r A_H(r)\,dr + n_{Z_H}(r), \tag{B.1}$$

$$Z_{\mathrm{DRm}}(r) = Z_{\mathrm{DR}}(r) - 2\times 10^{-3}\int_r A_{\mathrm{DP}}(r)\,dr + n_{Z_{\mathrm{DR}}}(r), \tag{B.2}$$

$$\Phi_{\mathrm{DPm}}(r) = 2\times 10^{-3}\int_r K_{\mathrm{DP}}(r)\,dr + n_{\Phi_{\mathrm{DP}}}(r), \tag{B.3}$$

where ZH, ZDR, and KDP are equivalent reflectivity factor at horizontal polarization, differential reflectivity, and differential propagation phase, respectively. Terms AH and ADP are precipitation attenuations for ZH and ZDR, respectively. And nZHm, nZDRm, and nΦDPm are random variables corresponding to the statistical properties of ZHm, ZDRm, and ΦDPm, respectively. Thus, ZHm, ZDRm, and ΦDPm are also random variables in the NTR. Terms ZH, ZDR, KDP, AH, and ADP are expressed by DSD, N(D), as

$$\zeta_h(r) = \frac{\lambda^4}{\pi^5|K_w|^2}\int_D 4\pi|s_{\mathrm{hh}}(D)|^2 N(D,r)\,dD; \quad (\mathrm{mm^6\,m^{-3}}), \tag{B.4}$$

$$\zeta_{\mathrm{dr}}(r) = \frac{\int_D |s_{\mathrm{hh}}(D)|^2 N(D,r)\,dD}{\int_D |s_{\mathrm{vv}}(D)|^2 N(D,r)\,dD}, \tag{B.5}$$

$$K_{\mathrm{DP}}(r) = \frac{180\lambda}{\pi}\int_D \mathrm{Re}[f_{\mathrm{hh}}(D) - f_{\mathrm{vv}}(D)]N(D,r)\,dD; \quad (\mathrm{deg\,km^{-1}}), \tag{B.6}$$

$$A_H(r) = 8.68\lambda\int_D \mathrm{Im}[f_{\mathrm{hh}}(D)]N(D,r)\,dD; \quad (\mathrm{dB\,km^{-1}}), \tag{B.7}$$

$$A_{\mathrm{DP}}(r) = 8.68\lambda\int_D \mathrm{Im}[f_{\mathrm{hh}}(D) - f_{\mathrm{vv}}(D)]N(D,r)\,dD; \quad (\mathrm{dB\,km^{-1}}), \tag{B.8}$$

where $\zeta_h(r) = 10^{0.1Z_H}$ and $\zeta_{\mathrm{dr}}(r) = 10^{0.1Z_{\mathrm{DR}}}$. Terms shh,vv(D) are backscattering amplitudes at horizontal and vertical polarizations, and fhh,vv(D) are forward-scattering amplitudes at horizontal and vertical

polarizations, respectively. Terms $\mathrm{Re}[\bullet]$ and $\mathrm{Im}[\bullet]$ are a real part and an imaginary part, respectively. Term λ is the wavelength of transmitting electromagnetic wave (mm). Term Kw is defined by a complex index of refraction of water ε as

$$K_w = \frac{\varepsilon^2 - 1}{\varepsilon^2 + 2}. \tag{B.9}$$

In the NTR, N(D) is defined by the normalized gamma DSD (Ulbrich 1983; Testud et al. 2001) to describe the natural variability of the DSD, as below:

$$N(D) = N_w f(\mu) \left(\frac{D}{D_0}\right)^{\mu} \exp(-\Lambda D); \quad (\mathrm{mm}^{-1}\,\mathrm{m}^{-3}), \tag{B.10}$$

where

$$\Lambda = \frac{3.67 + \mu}{D_0}, \tag{B.11}$$

$$f(\mu) = \frac{6}{3.67^4} \frac{(3.67 + \mu)^{\mu+4}}{\Gamma(\mu + 4)}, \tag{B.12}$$

and D is a diameter of a raindrop (mm), Nw is an intercept parameter (mm−1 m−3), D0 is a median volume diameter (mm), μ is a shape factor that is dimensionless, and $\Gamma(\bullet)$ is a gamma function.

B.1.2. SRR

This subsection describes the SRR, whose details are elaborated in Yoshikawa et al. (2014). The SRR is implemented as the preprocessing of the NTR, as shown in Fig. b.1. The SRR is an iterative ML approach to fit a range profile of the DSD parameters to dual-polarization measurements. A likelihood function of a range profile in the mth beam of the lth radar node is expressed as

$$p(\mathbf{y}^{(m,l)} \mid \mathbf{x}^{(m,l)}) = \mathcal{N}(\mathbf{y}^{(m,l)} \mid \mathbf{F}(\mathbf{x}^{(m,l)}), \mathbf{\Sigma}_y^{(m,l)}); \quad (m = 1, \ldots, M, \quad l = 1, \ldots, L), \tag{B.13}$$

where $\mathcal{N}(\mathbf{x} \mid \mathbf{m}_x, \mathbf{S}_x)$ is a Gaussian PDF whose mean vector and covariance matrix are represented as mx and Sx, respectively. Terms x(m,l) and y(m,l) are the range profiles of the DSD parameters and the dual-polarization measurements, respectively. Term F(x(m,l)) is the relation between x(m,l) and y(m,l), corresponding to Eqs. (1)–(12). Term Σy(m,l) is a covariance matrix of y(m,l), which is assumed to be known. Term M is the number of beams, and L is the number of radar nodes in the radar network. Terms x(m,l) and y(m,l) are represented as follows:

$$\mathbf{x}^{(m,l)} = (N_w'^{(1)}, \ldots, N_w'^{(n)}, \ldots, N_w'^{(N)}, D_0'^{(1)}, \ldots, D_0'^{(n)}, \ldots, D_0'^{(N)}, \mu')^{(m,l)} \tag{B.14}$$

$$\mathbf{y}^{(m,l)} = (Z_{\mathrm{Hm}}^{(1)}, \ldots, Z_{\mathrm{Hm}}^{(n)}, \ldots, Z_{\mathrm{Hm}}^{(N)}, Z_{\mathrm{DRm}}^{(1)}, \ldots, Z_{\mathrm{DRm}}^{(n)}, \ldots, Z_{\mathrm{DRm}}^{(N)}, \Phi_{\mathrm{DPm}}^{(1)}, \ldots, \Phi_{\mathrm{DPm}}^{(n)}, \ldots, \Phi_{\mathrm{DPm}}^{(N)})^{(m,l)} \tag{B.15}$$

where the superscript n indicates a parameter in the nth range bin rn of N range bins. Terms N'w, D'0,and μ' are applied as state variables, which are defined to avoid physical impossibilities through the iterative process,

$$N'_w(r) = \ln N_w(r), \tag{B.16}$$

$$D'_0(r) = \ln D_0(r), \tag{B.17}$$

$$\mu' = \frac{6}{1+\exp(-\mu_C)} - 1, \tag{B.18}$$

where μ is assumed to be a constant value, μC, in whole range of a radar beam as

$$\mu(r) = \mu_C. \tag{B.19}$$

Thus, Nw and D0 are kept positive and μ is squashed from −1 to 5 without any constraints to N'w, D'0, and μ'. In summary, the SRR solution, $\tilde{\mathbf{x}}^{(m,l)}$, is calculated by minimizing a cost function, which is derived from the likelihood function of Eq. (13), as shown below:

$$\begin{aligned} J(\mathbf{x}^{(m,l)}) &\equiv -\ln p(\mathbf{y}^{(m,l)} \mid \mathbf{x}^{(m,l)}) \\ &\propto \frac{1}{2}\sum_{n=1}^{N}\frac{(Z_{\mathrm{Hm}}^{(n)} - \hat{Z}_{\mathrm{Hm}}^{(n)})^2}{\sigma_{Z_H}^2} + \frac{1}{2}\sum_{n=1}^{N}\frac{(Z_{\mathrm{DRm}}^{(n)} - \hat{Z}_{\mathrm{DRm}}^{(n)})^2}{\sigma_{Z_{\mathrm{DR}}}^2} \\ &+ \frac{1}{2}\sum_{n=1}^{N}\frac{(\Phi_{\mathrm{DPm}}^{(n)} - \hat{\Phi}_{\mathrm{DPm}}^{(n)})^2}{\sigma_{\Phi_{\mathrm{DP}}}^2} \to \min, \end{aligned} \tag{B.20}$$

where σZH, σZDR, and σΦDP are standard deviations for each dual-polarization measurement, respectively, which are diagonal elements of Σy(m,l). The iterative minimization is reasonably converged by the Gauss–Newton (GN) method (Nocedal and Wright 1999).

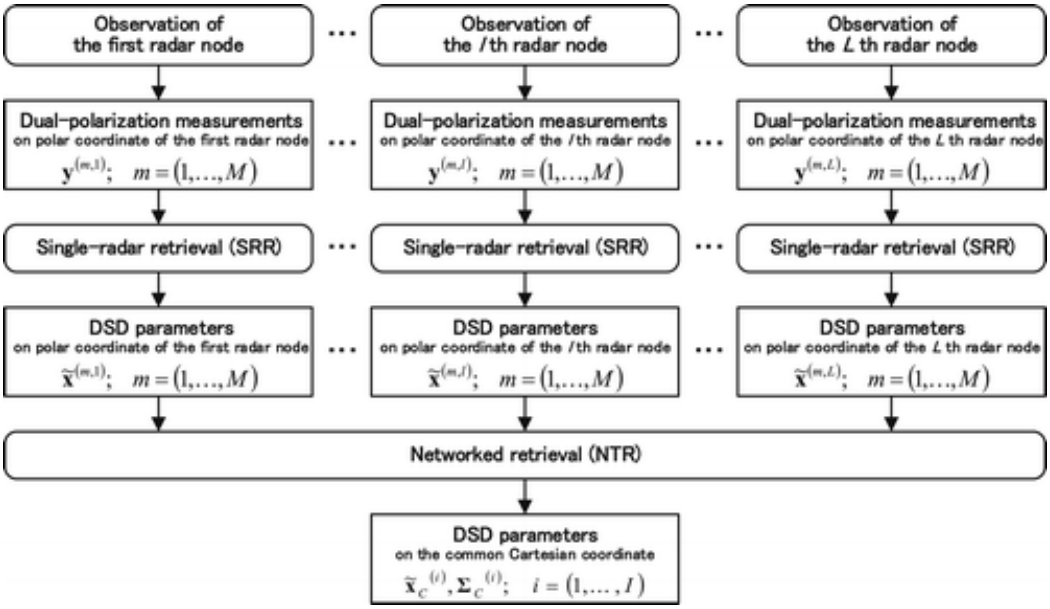

Figure b.1, Processing flow of DSD retrieval through the observation, the SRR, and the NTR.

B.1.3 NTR

A flowchart of the NTR is shown in Fig. b.2, which indicates that the NTR integrates the SRR solutions through three steps.

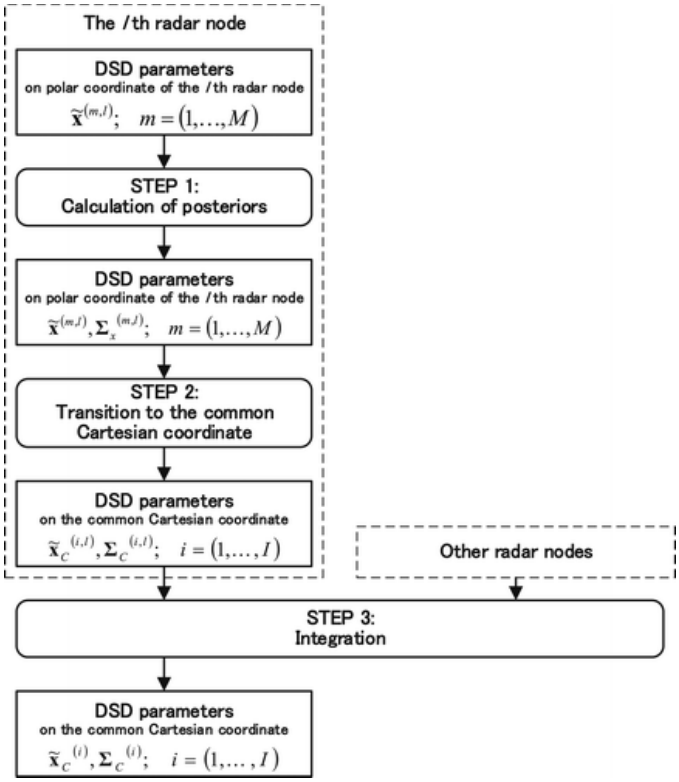

Figure b.2, Flowchart of the NTR

In step 1, posterior PDFs in each radar node are calculated from the SRR solutions. Step 2 transforms the posterior PDFs on the radar polar coordinate of each radar node to those on the common Cartesian coordinate defined in the radar network. In step 3, the posterior PDFs of each radar node on the common Cartesian grid are integrated optimally in a Gaussian stochastic sense.

1) Step 1: Posteriors of radar node

A posterior PDF in the mth beam of the lth radar node is theoretically derived by the product of a likelihood function and a prior PDF as

$$p(\mathbf{x}^{(m,l)} \mid \mathbf{y}^{(m,l)}) \propto p(\mathbf{y}^{(m,l)} \mid \mathbf{x}^{(m,l)}) p(\mathbf{x}^{(m,l)}). \qquad \text{(B.21)}$$

With a linear approximation of $\mathbf{F}(\mathbf{x}(m,l))$ around $\tilde{\mathbf{x}}^{(m,l)}$, the likelihood function of Eq. (13) is transformed as

$$p(\mathbf{y}^{(m,l)} \mid \mathbf{x}^{(m,l)}) \approx \mathcal{N}(\mathbf{F}'(m,l) \mid \mathbf{x}^{(m,l)} \mathbf{x}^{(m,l)}, \boldsymbol{\Sigma}_y^{(m,l)});$$
$$(m=1,\ldots,M, \quad l=1,\ldots,L), \qquad \text{(B.22)}$$

where

$$\mathbf{F}'^{(m,l)} = \left.\frac{\partial \mathbf{F}(\mathbf{x}^{(m,l)})}{\partial \mathbf{x}^{(m,l)}}\right|_{\mathbf{x}^{(m,l)}=\tilde{\mathbf{x}}^{(m,l)}}. \quad \text{(B.23)}$$

Supposing a situation without any other prior information, a noninformative PDF,

$p_{\text{no-info}}(\mathbf{x}) \equiv \mathcal{N}(\mathbf{x} \mid \mathbf{0}, \alpha\mathbf{I})(\alpha \to \infty)$, is applied to the prior PDF. Thus, Eq. (B.21) is transformed as

$$p(\mathbf{x}^{(m,l)} \mid \mathbf{y}^{(m,l)}) \approx \mathcal{N}(\mathbf{x}^{(m,l)} \mid \tilde{\mathbf{x}}^{(m,l)}, \boldsymbol{\Sigma}_x^{(m,l)}), \quad \text{(B.24)}$$

where

$$\boldsymbol{\Sigma}_x^{(m,l)} = (\mathbf{F}'^{(m,l)\mathrm{T}} \boldsymbol{\Sigma}_y^{(m,l)-1} \mathbf{F}'^{(m,l)})^{-1}. \quad \text{(B.25)}$$

Assuming that range profiles of DSD parameters are independent of each other, the posterior PDF, including all the beams of the lth radar node, is expressed as

$$p(\mathbf{x}^{(l)} \mid \mathbf{y}^{(l)}) \approx \mathcal{N}(\mathbf{x}^{(l)} \mid \tilde{\mathbf{x}}^{(l)}, \boldsymbol{\Sigma}_x^{(l)}), \quad \text{(B.26)}$$

where

$$\tilde{\mathbf{x}}^{(l)} = [\tilde{\mathbf{x}}^{(1,l)\mathrm{T}} \quad \dots \quad \tilde{\mathbf{x}}^{(M,l)\mathrm{T}}]^{\mathrm{T}} \quad \text{(B.27)}$$

$$\boldsymbol{\Sigma}_x^{(l)} = \mathrm{diag}(\boldsymbol{\Sigma}_x^{(1,l)} \quad \dots \quad \boldsymbol{\Sigma}_x^{(M,l)}). \quad \text{(B.28)}$$

2) Step 2: Transitions to a common Cartesian grid

A posterior PDF in the lth radar node on the lth radar polar coordinate is transited to that on a common Cartesian coordinate, as shown below:

$$\begin{aligned} p(\mathbf{x}_C^{(i)} \mid \mathbf{y}^{(l)}) &\equiv \mathcal{N}(\mathbf{x}_C^{(i)} \mid \tilde{\mathbf{x}}_C^{(i,l)}, \boldsymbol{\Sigma}_C^{(i,l)}) \\ &= \mathcal{N}(\mathbf{x}_C^{(i)} \mid \mathbf{T}^{(i,l)} \tilde{\mathbf{x}}^{(l)}, \mathbf{T}^{(i,l)} \boldsymbol{\Sigma}_x^{(l)} \mathbf{T}^{(i,l)\mathrm{T}}), \end{aligned} \quad \text{(B.29)}$$

where xC(i) is a vector including the two DSD parameters in the ith grid of I common Cartesian grids, defined as

$$\mathbf{x}_C^{(i)} = [N_w', D_0']^{(i)^{\mathrm{T}}}; \quad (i = 1, \dots, I). \quad \text{(B.30)}$$

Note that μ' is omitted because the SRR does not consider a range profile of μ. Term T(i,l) is a transition matrix from a polar coordinate of the lth radar node to the ith grid of the common Cartesian grid. Transition methods from polar to Cartesian coordinates have been described (Trapp and Doswell 2000). The closest-point method, which is primitive in radar meteorology, is applied in this paper. Equation (29) indicates that other linear transition methods can be alternated.

3) Step 3: Integration

Posterior PDFs of all the radar nodes on the common Cartesian coordinate have now been prepared. Assuming that posterior PDFs calculated by each radar node are independent and identically distributed (i.i.d), their joint distribution is theoretically given as

$$p\left(\mathbf{x}_C^{(i)} \middle| \mathbf{y}^{(1)} \quad \cdots \quad \mathbf{y}^{(L)}\right) \equiv \mathcal{N}(\mathbf{x}_C^{(i)} \mid \tilde{x}_C^{(i)}, \mathbf{\Sigma}_C^{(i)}) = \prod_{l=1}^{L} p(\mathbf{x}_C^{(i)} \mid \mathbf{y}^{(l)}), \tag{B.31}$$

where

$$\tilde{\mathbf{x}}_C^{(i)} = \left(\sum_{l=1}^{L} \mathbf{\Sigma}_C^{(i,l)-1} \right)^{-1} \left(\sum_{l=1}^{L} \mathbf{\Sigma}_C^{(i,l)-1} \tilde{\mathbf{x}}_C^{(i,l)} \right) \tag{B.32}$$

$$\mathbf{\Sigma}_C^{(i)} = \left(\sum_{l=1}^{L} \mathbf{\Sigma}_C^{(i,l)-1} \right)^{-1}. \tag{B.33}$$

Thus, the integrated solution $\tilde{\mathbf{x}}_C^{(i)}$ is the best solution of the radar network in a Gaussian stochastic sense.

B.2. Evaluation by numerical simulation

B.2.1. Specifications of numerical simulation

Numerical simulations of the NTR are carried out to confirm their performance. Two-dimensional distributions of reference values of the DSD parameters are shown in Fig. b.3, where Nw and D0 are in Figs. b.3a and 3b, respectively. The reference values of Nw and D0 were generated from observed data on the Colorado State University–University of Chicago–Illinois State Weather Survey (CSU–CHILL) radar. The observation was carried out on 20 June 2000. The area shown in Fig. b.3 is placed inside the area of the observation. The observed data were converted to the reference values of DSD parameters with the use of the algorithm proposed by Gorgucci et al. (2002). The algorithm by Bringi et al. (2002) was applied in cases where the obtained KDP was noisy. Since it is well known that μ varies depending on D0, a varying μ model is applied in order to simulate a natural variation of μ. The μ of each range bin is determined by a linear μ–D0 relation as

$$\mu = -\frac{\mu_u - \mu_l}{D_{0\max} - D_{0\min}} (D_0 - D_{0\min}) + \mu_u, \tag{B.34}$$

where D0max and D0min are the maximum and minimum D0 in the dataset, respectively. Terms μu and μl are the largest and smallest values in a horizontal profile of μ. In this section, 2.0 and −0.5 were selected for μu and μl, respectively. Observed parameters ZHm, ZDRm, and ΦDPm at a frequency of 9.5 GHz (X band) were calculated from these generated reference values of DSD parameters on the assumption of spheroidal raindrops with the axis ratio of the Beard and Chuang (BC) model (Beard and Chuang 1987). Then, normally distributed fluctuations were added to the three observed parameters, whose standard deviations are 0.8 dBZ, 0.2 dB, and 1.5°, respectively. These values of the standard deviations were chosen by referring to Bringi and Chandrasekar (2001, chapter 6), wherein the theoretical fluctuations in the dual-polarization measurements are derived. The "×" marks in both

panels of Fig. 3 indicate the positions of each radar node, which are assumed to be deployed with the same interval on a circle whose diameter is 30 km as connected by dashed lines. Numbers labeled at each radar node are noted beside each × mark. A square area bounded by the dotted line (its side length is about 21 km) is an area of interest in which DSD parameters are retrieved by the NTR. It is assumed that eight X-band radars are deployed on the field with a maximum observation range of 30 km and 1024 range bins; that is, each range bin is about 30 m long. A disagreement between polar coordinates of the CSU–CHILL radar and the assumed X-band radar was solved by linear interpolation.

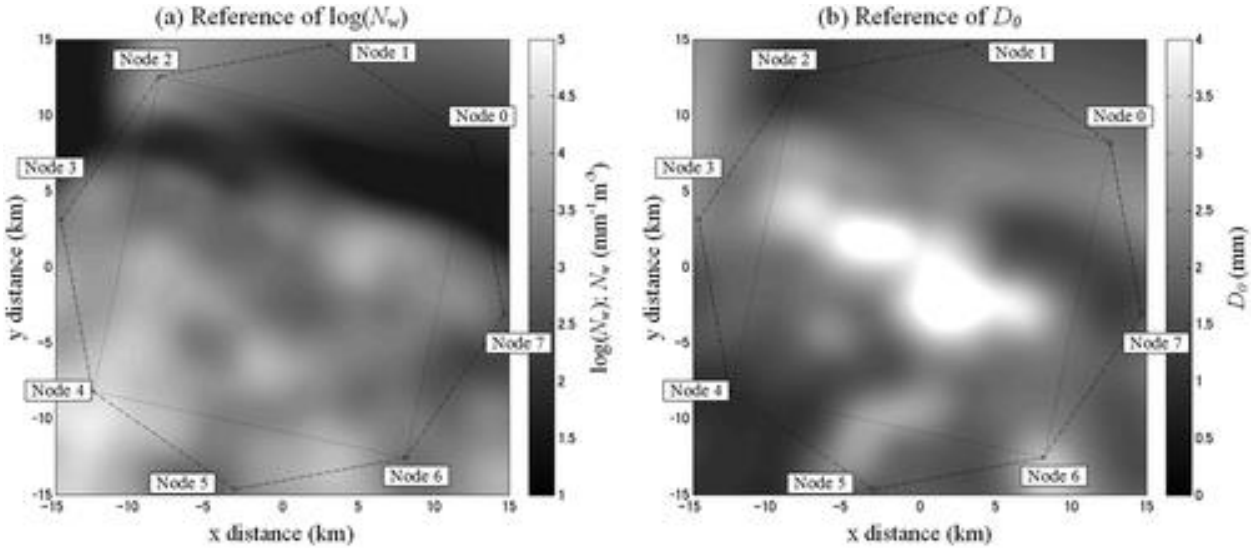

(a) (b)

Figure b.3, 2D distributions of reference values of DSD parameters: (a) reference of log(Nw) [Nw (mm−1 m−3)] (b) reference of D0 (mm). In each panel, "×" marks indicate the position of each radar node; nodes are located on a circle whose diameter is 30 km with the same interval as connected by dashed lines. Numbers labeled for each radar node are noted beside each × mark. A square area bounded by a dotted line is a target space.

In the proposed algorithm, the same assumptions as in the calculation of the dual-polarization measurements from the reference values of DSD parameters—spheroidal raindrops and the BC model—are applied (see Bringi and Chandrasekar 2001, chapter 4). In the zeroth step (the SRR), it is assumed in the algorithm that 16 adjacent range bins have the same DSD in order to reduce the effect of fluctuations in measurements and calculation costs. Thus, the algorithm has 64 state variables for both Nw and D0 in a radar beam. On the basis of this assumption, three measurements in a chunk of 16 range bins are calculated by one DSD, which means that solutions in this simulation have a range resolution of about 480 m. The iteration process of the GN method is stopped by a defined threshold of an iterating update or iteration count. These settings in the SRR are the same as in our previous work (Yoshikawa et al. 2014). An area of interest for the NTR is separated by 128 × 128 square grids. The closest-point

method is applied for transition to the common grid. All these settings of the simulation are summarized in Table b.1.

Table b.1, Simulation characteristics.

Radar	
Frequency	9.5 GHz
Coverage range	0–30 km
No. of range bins	1024
Fluctuations	Normal distributions with std dev of 0.8 dBZ, 0.2 dB, and 1.5° in Z_{Hm}, Z_{DRm}, and Φ_{DPm}, respectively
Simulated precipitation	
Dataset	269 range profiles of N_w and D_0 generated from data observed in the CSU–CHILL radar on 20 Jun 2000
DSD model	Normalized gamma DSD (Testud et al. 2001) with every 0.1-mm equivolume spherical diameter from 0.5 to 8.0 mm
Raindrop shape	Spheroid
Axis ratio model	PB, BC, or TB model
SRR	
No. of chunks of range bins	16
Raindrop shape	Spheroid
Axis ratio model	BC model
Stabilization factors (σ_{Nw}, σ_{D0})	(2.00, 3.00)
Convergence criteria	$\begin{pmatrix} \|\boldsymbol{\Delta}\mathbf{N}_w\|_i\|^2/\|\mathbf{N}_w\|_{i-1}\|^2 < 10^{-6} \\ \|\boldsymbol{\Delta}\mathbf{D}_0\|_i\|^2/\|\mathbf{D}_0\|_{i-1}\|^2 < 10^{-6} \\ \|\Delta\mu_C\|_i\|^2/\|\mu_C\|_{i-1}\|^2 < 10^{-6} \end{pmatrix}$ or $i = 2M + 1$, where $\mathbf{x}\|_{i-1}$ is a vector of a DSD profile in the $i-1$th iteration and $\boldsymbol{\Delta}\mathbf{x}\|_i$ is an update vector of a DSD profile in the GN method. Term M is the number of chunks of range bins (=64 in this paper).
NTR	
Integrated 2D grid field	128 × 128 grids in 21 km × 21 km
Number of radar nodes	2, 4, and 8

The integration of the NTR is performed in each common Cartesian grid as shown in Eq. (B.31); that is, 16 384 retrievals of the NTR are evaluated in the single 2D distribution of precipitation. In addition, the dataset of DSD parameters is the same as the one used in our previous work (Yoshikawa et al. 2014), where it is indicated that the statistical properties of the reference values almost agree with a long-term observational result by a Joss–Waldvogel disdrometer [see Fig. 2 in Yoshikawa et al. (2014) and Fig. 7.17 in Bringi and Chandrasekar (2001)]. Therefore, this numerical simulation covers a wide range of precipitation and includes a sufficient number of attempts to confirm the theoretical performance of the NTR.

B.2.2. Improvement from the SRR

Figure b.4 shows the retrieved results. Figures b.4a and b.4b are horizontal distributions of Nw retrieved by the SRR on nodes 0 and 4, respectively, and Figs. b.4d and 4e are those of D0. The NTR results of Nw and D0 are shown in Figs. b.4c and 4f respectively, where they are retrieved by the NTR integration with nodes 0 and 4 (2-NTR), respectively. On the upper sides of Figs. b.4a and b.4d which indicate a weak precipitation region, discontinuities along the azimuth direction significantly appear. The ZH are roughly 25–31 dBZ in this area, which is reasonable to make the SRR unstable. Compared with the reference shown in Fig. b.3, the retrievals in this area have larger errors than ones in the other areas. As seen in Figs. b.4c and b.4f, the NTR properly corrects the discontinuity in the upper area of node 0.

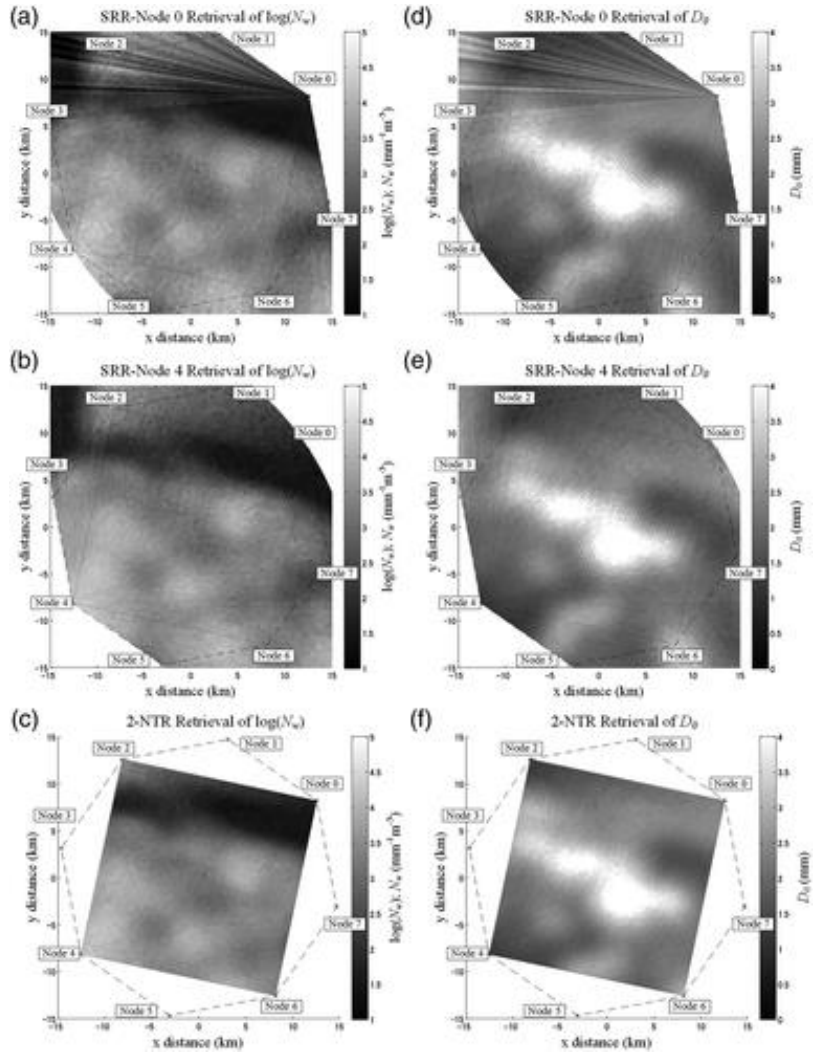

Figure b.4, 2D distributions of retrieved DSD parameters: (a) the SRR retrievals of Nw in node 0, (b) the SRR retrievals of Nw in node 4, (c) the NTR retrievals of Nw with nodes 0 and 4, (d) the SRR retrievals of D0 in node 0, (e) the SRR retrievals of D0 in node 4, and (f) the NTR retrievals of D0 with nodes 0 and 4.

Figure b.5, showing horizontal distributions of standard deviations of the SRR solutions of nodes 0 and 4 (corresponding to the square roots of the diagonal elements of $\boldsymbol{\Sigma}_x^{(0)}$ and $\boldsymbol{\Sigma}_x^{(4)}$, respectively), indicates how integration of the NTR works. Figures 5a–5d show those of Nw in node 0, Nw in node 4, D0 in node 0, and D0 in node 4, respectively. As pointed out in Yoshikawa et al. (2014), the SRR is unstable in the case of weak precipitation throughout a beam because the DSD parameters have less sensitivity to the dual-polarization measurements in such a case due to a characteristic of the nonlinear function expressed in Eqs. (B.1)–(B.12). However, the covariance matrix, $\boldsymbol{\Sigma}_x^{(I)}$, includes large variances in the diagonal elements corresponding to those unstable solutions. This is seen in the upper side of Figs. b.5a and b.5c. In the NTR, the DSD parameters are integrated considering each covariance based on a Bayesian scheme—that is, an accurate solution is obtained as long as one node in a radar network has a stable solution by the NTR utilizing a multidirectional observation environment. On the other hand, in the case of all nodes

having a stable solution in a desired grid, the SRR retrievals in each node are integrated with almost equivalent averaging to derive retrieval with lower fluctuations.

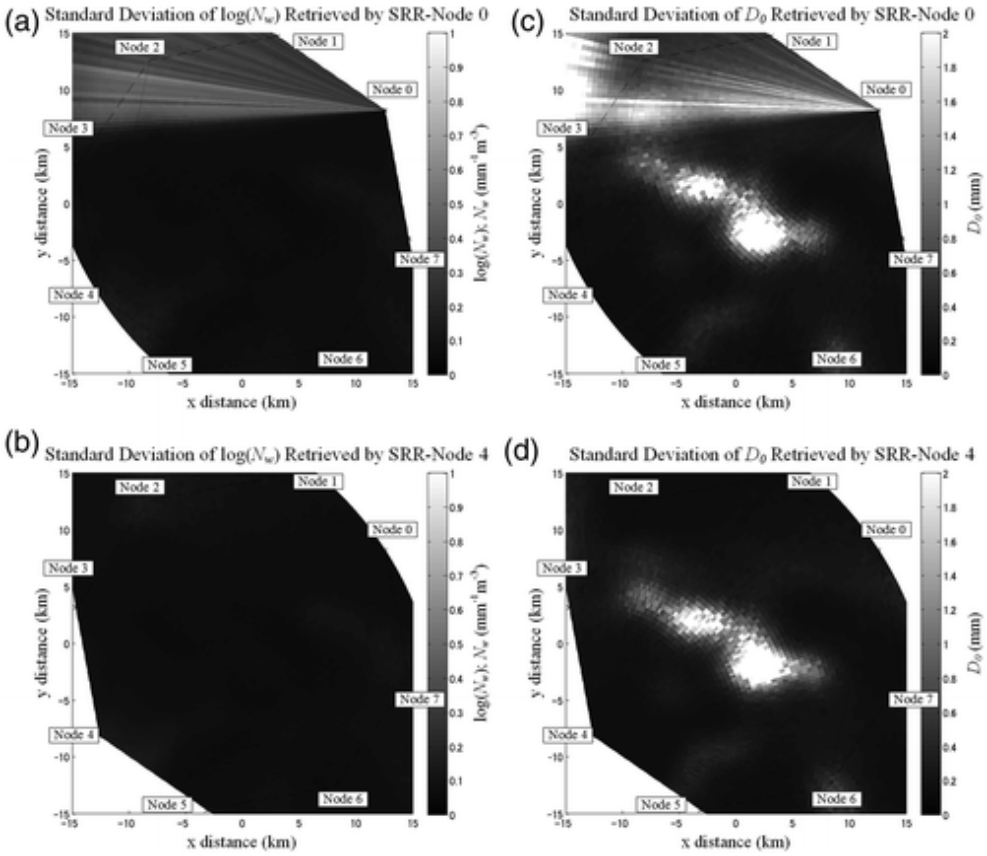

Figure b.5 2D distributions of standard deviations of the SRR solutions: (a) the standard deviations of Nw in node 0, (b) the standard deviations of Nw in node 4, (c) the standard deviations of D0 in node 0, and (d) the standard deviations of D0 in node 4.

B.2.3. Error analyses

To confirm the performance of the NTR with possible radar network situations, statistical evaluations are carried out by changing setting parameters of the numerical simulation with respect to the number of radar nodes, ranges of varying μ, axis ratio models, and system bias errors. Hereafter, 8-NTR is implemented on the assumption that the BC axis ratio model is applied, 2.0 and −0.5 are selected for μu and μl of the μ model, respectively, and no system bias error is considered in all the radar nodes if not specified. Throughout the error analyses, evaluated bias and standard errors are summarized in Table 2.

Table b.2 Bias and standard errors of log(Nw) [Nw (mm−1 m−3)] and D0 (mm) resulting from the numerical simulations; bias error (standard error). Standard setting; 8-NTR, (μu, μl) = (2.0, −0.5), BC model, and no-biased measurements. In the others, the standard setting is applied if not specified.

	$\log(N_w)$	D_0
Standard setting	−0.05 (0.09)	0.04 (0.09)
2-NTR	−0.05 (0.12)	0.03 (0.12)
4-NTR	−0.05 (0.10)	0.04 (0.09)
$(\mu_u, \mu_l) = (0.0, 0.0)$	−0.00 (0.05)	0.00 (0.06)
$(\mu_u, \mu_l) = (5.0, -1.0)$	−0.10 (0.14)	0.07 (0.13)
PB model	−0.11 (0.15)	0.12 (0.12)
TB model	−0.22 (0.21)	0.16 (0.24)
Randomly biased	−0.09 (0.15)	0.07 (0.14)

1) Number of radar nodes

The 2- and 4-NTR, where nodes 0 and 4 and nodes 0, 2, 4, and 6 were applied, respectively, were compared to the 8-NTR. In Fig. b.6, bias and standard errors of Nw and D0 calculated by comparing the NTR results with the reference values are shown. Figures b.6a and b.6b correspond to those of Nw and D0, respectively. Each panel indicates bias and standard errors separately calculated in six different quantiles of each DSD parameter (i.e., <2, 2–2.5, 2.5–3, 3–3.5, 3.5–4, >4 for log(Nw), and 0–1.5, 1.5–2, 2–2.5, 2.5–3, 3–3.5, >3.5 for D0.) For example, in Fig. b.6a, the three biases and standard errors in the leftmost row are those with reference values of log(Nw) less than 2. Dotted, dashed, and solid lines are bias and standard errors, represented with the vertical bars of the 2-, 4-, and 8-NTRs, respectively. For clarification purposes, the lines of bias and standard errors are plotted with slight shifts along the horizontal axis. Bias errors are equivalent among the NTRs through all the quantiles of each DSD parameters. Smaller standard errors appear by increasing the number of radar nodes. Table b.2 also indicates that bias errors of the 2-, 4-, and 8-NTRs are −0.05 in log(Nw) and either 0.03 or 0.04 in D0. The standard errors of the 2-, 4-, and 8-NTRs are 0.12, 0.10, and 0.09 in log(Nw) and 0.12, 0.09, and 0.09 in D0, respectively. This is apparently because the NTR is based on a Bayesian scheme where a greater number of observed samples decrease uncertainties in state variables.

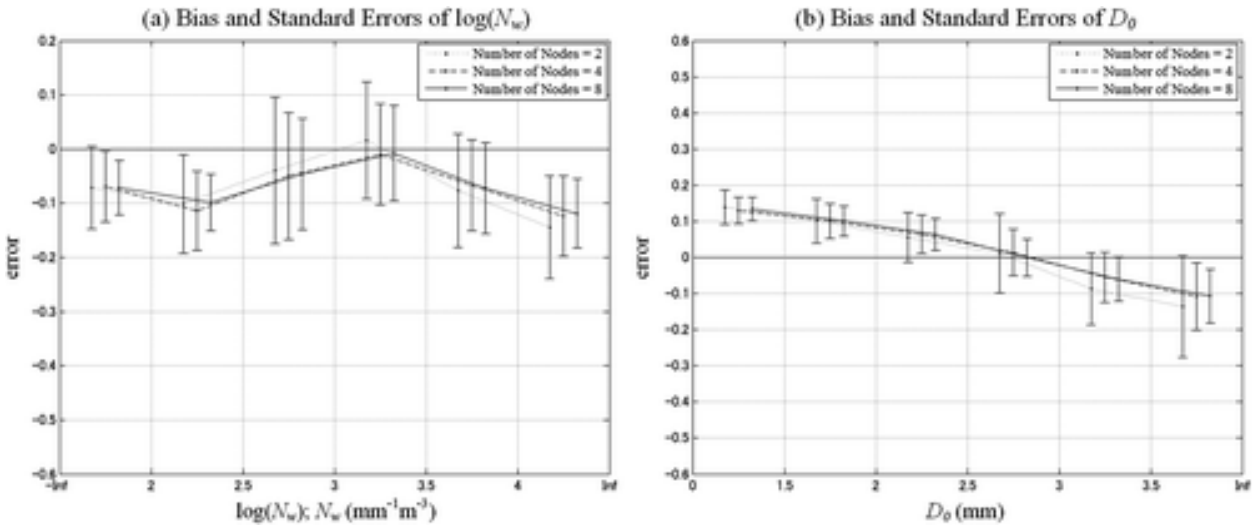

(a) (b)

Figure b.6, Result of error analysis with regard to the number of the radar nodes. Bias and standard errors of (a) log(Nw) and (b) D0. The errors are represented with six different quantiles (i.e., <2, 2–2.5, 2.5–3, 3–3.5, 3.5–4, >4 for log(Nw), and 0–1.5, 1.5–2, 2–2.5, 2.5–3, 3–3.5, >3.5 for D0.) In each panel, the dotted, dashed, and solid lines correspond to the 2-, 4-, and 8-NTR, respectively (lines are drawn with slight shifts for clarity).

2) Ranges of varying μ

Varying μ of the actual precipitation could give significant errors to the NTR since constant μ is assumed in each radar beam in the zeroth step (SRR). To evaluate those errors, dual-polarization measurements were calculated with three different ranges of varying μ, where μu and μl are 1) 0.0 and 0.0; 2) 2.0 and −0.5; and 3) 5.0 and −1.0, respectively.The second μ range is the same one as in section 3a. These values of μu and μl were prepared by referring to Ulbrich and Atlas (1998) and Moisseev and Chandrasekar (2007). The expression (μu, μl) = (0.0, 0.0) results in a constant μ model and is equivalent to the Marshall–Palmer DSD (Marshall and Palmer 1948). In Fig. b.7, bias and standard errors of Nw and D0 are shown. Dotted, dashed, and solid lines correspond to μ ranges 1–3, respectively. With the μ range 1, the NTR outputs retrievals with bias and standard errors of −0.00 and 0.05 in log(Nw), and 0.00 and 0.06 in D0, respectively, which are the best accuracy throughout the error analysis, as shown in Table b.2. The bias errors occur only because of spatial disagreements between the reference and the NTR. While the reference values of DSD parameters were calculated on the common Cartesian coordinate, dual-polarization measurements in each radar node were calculated from DSD parameters on each radar polar coordinate. Then the standard deviations are due to a combination of the coordinate disagreement and the fluctuations in the dual-polarization measurements. Errors due to the constant μ assumption of the SRR appear in the μ ranges 2 and 3, as shown in Fig. b.7, where μ monotonically decreases along D0. This is because of the disagreement of the SRR's assumption of constant μ with the spatial variation of μ. Both bias and standard errors increase with a higher variation of μ. Table b.2

indicates that evaluation with the μ range 3 outputs the largest bias and standard errors in the three μ ranges, which are −0.10 and 0.14 in log(Nw), and 0.07 and 0.13 in D0, respectively These evaluated values are possibly the worst errors caused by the variation of μ because varying μ from −1.0 to 5.0 is naturally too large to exist in the entire target area.

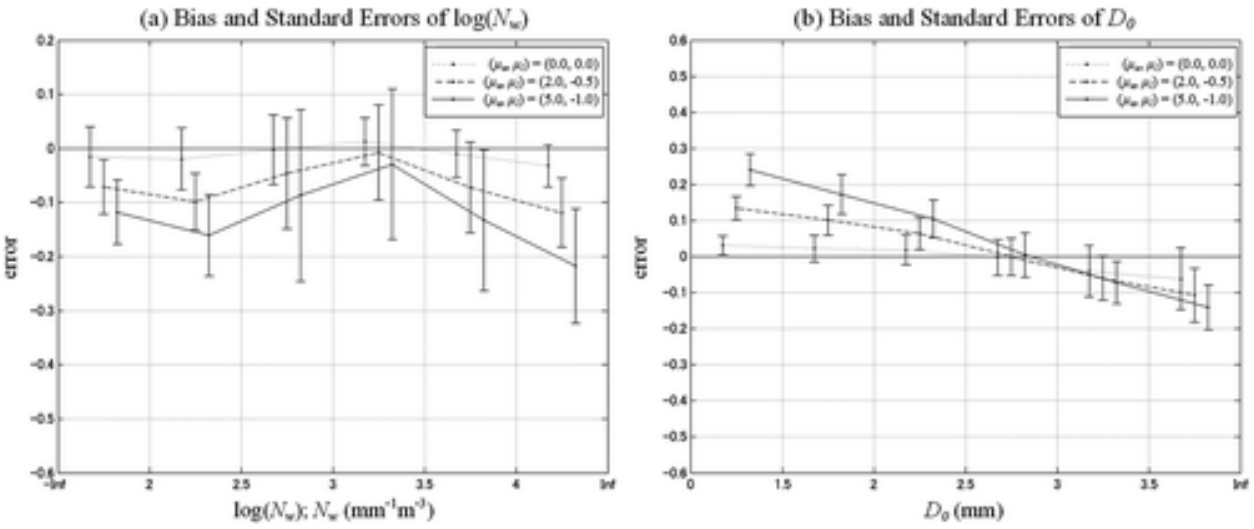

(a) (b)

Figure b.7, Result of error analysis with regard to the ranges of varying μ. Bias and standard errors of (a) log(Nw) and (b) D0. The errors are represented with six different quantiles (i.e., <2, 2–2.5, 2.5–3, 3–3.5, 3.5–4, >4 for log(Nw), and 0–1.5, 1.5–2, 2–2.5, 2.5–3, 3–3.5, >3.5 for D0.) In each panel, the dotted, dashed, and solid lines correspond to the three μ ranges with μu and μl of 0.0 and 0.0, 2.0 and −0.5, and 5.0 and −1.0, respectively (lines are drawn with slight shifts for clarity).

3) Axis ratio models

Errors caused by incompatibility of the axis ratio between the NTR assumption (the BC model used in this paper) and actual precipitation were confirmed in this subsection. Two numerical simulations where dual-polarization measurements were calculated using the Pruppacher and Beard (PB) model (Pruppacher and Beard 1970) and the Thurai and Bringi (TB) model (Thurai and Bringi 2005) are compared with the BC model. In Fig.b. 8, the bias and standard errors of Nw and D0 are shown. Dotted, dashed, and solid lines correspond to the PB, TB, and BC models, respectively. As in the error analysis of the μ range, it is seen in Fig. b.8b that the bias error of the PB and TB models monotonically depend on D0. This is because an axis ratio is a function of D. In the simulation with the PB model, the bias and standard errors are −0.11 and 0.15 in log(Nw), and 0.12 and 0.12 in D0, respectively. In the TB model, those errors are −0.22 and 0.21 in log(Nw), and 0.16 and 0.24 in D0, respectively. According to Table b.2, the bias and standard errors could be affected up to 2 times greater than those of the varying μ from

−1.0 to 5.0. Note that the area of interest is too large to have precipitation with a uniform axis ratio model. Therefore, the evaluated bias and standard errors are the possible worst errors caused by the axis ratio model.

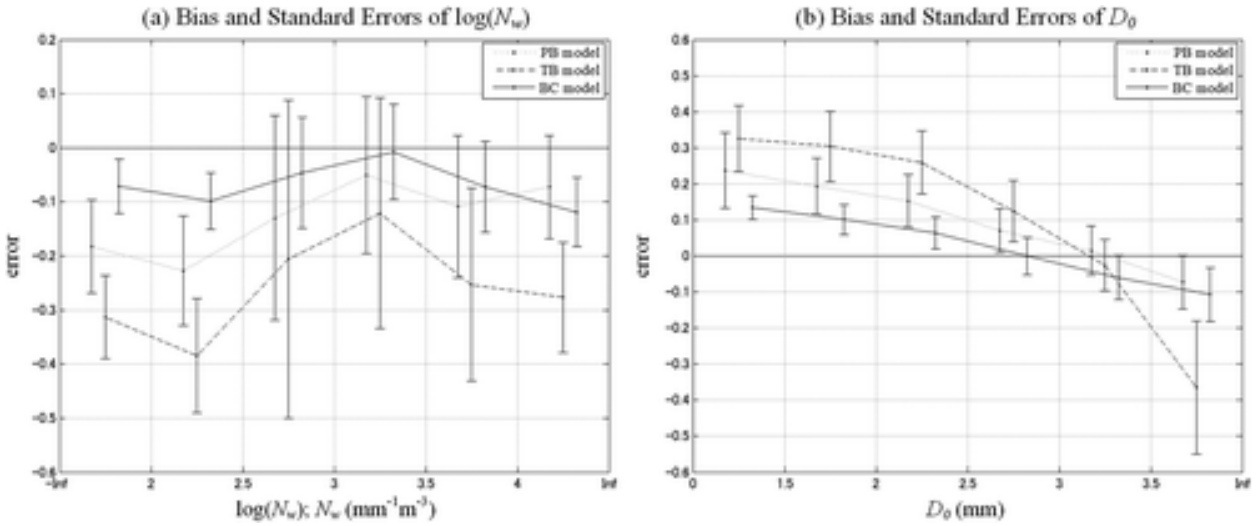

(a) (b)

Figure b.8, Result of error analysis with regard to the axis ratio models. Bias and standard errors of (a) log(Nw) and (b) D0. The errors are represented with six different quantiles (i.e., <2, 2–2.5, 2.5–3, 3–3.5, 3.5–4, >4 for log(Nw), and 0–1.5, 1.5–2, 2–2.5, 2.5–3, 3–3.5, >3.5 for D0.) In each panel, the dotted, dashed, and solid lines correspond to the PB, TB, and BC models, respectively (lines are drawn with slight shifts for clarity).

4) System bias errors

Radars may have system bias errors in their measurements from several causes such as a water-coated radome, temperature-dependent amplifier gain, and so on. Although these kinds of errors are typically calibrated in the quality control process, it is difficult to correct them completely. To make an error analysis of this problem, the ZHm and ZDRm of all eight nodes were independently and randomly biased. Bias values of ZHm were generated by a Gaussian random number generator with a mean value of 0 dBZ and a standard deviation of 1 dBZ. Random biases with a mean value of 0 dB and a standard deviation of 0.2 dB were given for ZDRm. Note that the measurements are biased by the same value in an arbitrary radar node. Twenty independent simulations of 8-NTR showed that the bias and standard errors of log(Nw) are −0.09 and 0.15, and that those of D0 are 0.07 and 0.14, respectively. As shown in Table 2, these system biases could give almost 2 times worse bias errors and about 1.5 times worse standard errors than the standard setting in both log(Nw) and D0 retrievals.

B.3. Conclusions

An integrated DSD retrieval algorithm for an X-band dual-polarization radar network is proposed. The proposed algorithm, the NTR, is based on our previous work, which is a DSD retrieval method on a single radar, the SRR (Yoshikawa et al. 2014). The NTR is configured with the three steps, as below. In the preface, the SRR is implemented in all the radar beams of all the radar nodes included in a radar network. In the first step, the SRR solutions in each radar node are transformed to a posterior PDF; that is, a covariance matrix of the SRR solutions is calculated from known error covariance by linearly approximating the governing equation around the SRR solution. In the second step, the SRR solutions and their covariance matrices are transited from polar gridded ones to a common Cartesian gridded one using a transition matrix. In the final step, the SRR solutions and their covariance matrices on the common Cartesian grid are integrated based on a Bayesian scheme. It is concluded that the integrated solution of the NTR is theoretically the best estimation in the Gaussian stochastic sense.

Numerical simulations were carried out to verify the estimation accuracy, supposing a radar network in which two, four, or eight X-band radars are deployed on a circle whose diameter is 30 km. The reference value of DSD parameters was created from the CSU–CHILL radar data. Dual-polarization radar measurements of each radar node were calculated from the reference values of DSD parameters on the assumption of a spheroid raindrop shape and a fixed axis ratio model (see Table 1 for details of setting parameters.) As described in Fig. b.4, the NTR properly corrects the wrong spatial discontinuities of the SRR, which is because the SRR retrieves DSD parameters in respect to each radar beam independently. Error analyses to evaluate the performance of the NTR in possible situations of a radar network were carried out. Specifically, statistical evaluations were implemented with the numerical simulation by changing the setting parameters of the numerical simulation with respect to the number of radar nodes, ranges of varying μ, axis ratio models, and system bias errors. Because the NTR is based on a Bayesian scheme, the number of radar nodes works to reduce standard errors in the retrievals. The constant μ assumption of the SRR yields bias and standard errors of −0.10 and 0.14 in log(Nw), and 0.07 and 0.13 in D0 with varying μ from −1.0 to 5.0, respectively. Incompatibility of axis ratio models between the NTR assumption and actual precipitation gives retrieval errors up to 2 times greater than varying μ from −1.0 to 5.0. Further, system bias errors of about 1 dBZ and 0.2 dB (both of which are root-mean-square values) in ZHm and ZDRm, respectively, give bias and standard errors of −0.09 and 0.15 in log(Nw), and 0.07 and 0.14 in D0, respectively. In actual observation, a natural combination of these error sources should be included, and each of the error sources could be heavier than the settings of the error analyses. Our future work will entail performance evaluations in the CASA experiment or the Midlatitude Continental Convective Clouds Experiment (MC3E) by comparing ground-based devices, such as disdrometers, with DSD parameters and rainfall rate.

The concept of the NTR can be expanded from a radar network to a multisensor network, and the expansion will be a part of our future work. In the case of a weather observation campaign, many kinds of sensors such as radars at several frequencies, rain gauges, and disdrometers are deployed. In general, ground-based devices are utilized as hard constraints, where radar-retrieved physical parameters of precipitation are corrected so as to exactly match a measurement of ground-based devices. However, a ground-based device would have uncertainty due to not only its accuracy but also gaps of positions and resolution volumes. Therefore, a hard constraint generally gives a bias error by neglecting those uncertainties. On the other hand, the concept of the NTR offers soft constraints based on a Bayesian

scheme, which appropriately improves radar-retrieved physical parameters of precipitation by considering both uncertainties of a radar retrieval and measurement of a ground-based device.

C. Characterizing falling snow using multifrequency dual-polarization measurements

Combinations of dual-polarization measurements at various radar frequencies and elevation angles together with realistic scattering computations of snowflakes are compared in order to study how they can be used to characterize falling snow. In the study, we use seven different ice crystal habits, including graupel, and different types of aggregates. The single-particle scattering is modeled using the discrete-dipole approximation, and the backscattering cross sections are integrated over exponential size distributions. We take advantage of statistical properties of the large set of scattering results to determine which combination of measurements provide overall best characterization of snow types. We find that a combination of the differential reflectivity and the depolarization ratios, especially in the circular basis, is useful in the characterization, while the dual-frequency ratios at higher frequencies than the Ku band are almost as good. Also, the assumption of preferential orientation for single ice crystals plays an important role when analyzing the results. These conclusions are tested against both airborne and ground-based radar measurements obtained during the Global Precipitation Measurement Cold-season Precipitation Experiment field campaign in 2012. The results show that dual-polarization and dual-frequency measurements provide complimentary information and can narrow down the characterization of falling snow considerably.

C.1. Numerical Methods

C.1.1 Shape Models for Snowflakes

Due to the importance of shape in scattering at the resonance regime (size parameter $x = ka > 1$, where $k = 2\pi/\lambda$ is the wave number and λ the wavelength of the incident wave, and a the volume-equivalent-sphere radius of the particle), it is advisable to use a physically realistic model for the various shapes for snowflakes and ice crystals (see section 1). In the present study, we use six different pristine ice crystal types: hexagonal column, hexagonal plate, needle, ordinary dendrite, fern-like dendrite, and six-bullet rosette, covering most of the more common types occurring at various atmospheric conditions and altitudes. In order to mimic natural shapes, we use the measured thickness-to-diameter and length-to-diameter ratios reported by Pruppacher and Klett [1997] for the different types of ice crystals (see Table c.1).

Needles are modeled as long circular cylinders, while for the dendrites, we use the crystal growth algorithm by Reiter [2005]. It is based on a 2-D cellular automaton using two parameters that control the amount of water available for the cells both locally and globally. This model was chosen mainly due

Table c.1 Snowflake Properties for the Computations

Snowflake Type	D_{max} (mm)	D_0 (mm)	Dimensions (cm)	Number of Crystals
Hexagonal column (N1e)	0.1–2.0	0.7–1.6	$d = 0.03527 L_{max}^{0.437}$	1
Hexagonal plate (P1a)	0.1–2.0	0.7–1.6	$h = 0.0141 D_{max}^{0.474}$	1
Needle (N1a)	0.3–3.0	1.6–2.2	$d = 0.030487 L_{max}^{0.61078}$	1
Ordinary dendrite (P1e)	0.4–4.3	2.1–3.4	$h = 0.009022 D_{max}^{0.377}$	1
Fernlike dendrite (P1f)	0.9–7.0	3.5–5.6	$h = 0.009022 D_{max}^{0.377}$	1
Six-bullet rosette (C3b)	0.2–1.4	0.7–1.1	$d = 0.0151 L_{max}^{0.455}$	1
Lump graupel (R4b)	0.5–5.0	2.0–4.0	–	–
Aggregate of needles	0.3–8.0	2.2–6.4	–	2, 10, 20, 30, 40, 50
Aggregate of ordinary dendrite	0.6–17.8	1.9–13.6	–	2, 10, 20, 30, 40, 50
Aggregate of fernlike dendrite	1.4–24.0	5.6–17.5	–	2, 10, 20, 30, 40, 50
Aggregate of rosettes	0.3–4.4	1.5–3.4	–	2, 5, 10, 15, 20

to its simplicity and physical basis, whereas some other models may be more realistic [Libbrecht, 2005; Gravner and Griffeath, 2009]. For the six-bullet rosettes, we adopted the shapes by Um and McFarquhar [2007], which are based on aircraft measurements from cirrus clouds.

For the purpose of comparison, we also include lump graupel generated with the fractal model by Ishimoto [2008]. In the fractal model, the snowflake is generated using an iterative method, which adds ice cells into a cubic lattice. The amount of ice added is controlled by two parameters: the fractal dimension fD and the total number of iterations. For generating graupel, the fractal dimension fD=2.7 was chosen in order to get a proper fit to the measured mass-diameter relationship by Heymsfield and Kajikawa [1987]. This value is also close to the maximum possible with the current implementation. For the number of iterations, we use 4, 5, 6, and 7.

To generate realistic aggregates, we use the physically based aggregation model by Westbrook [2004]. It mimics the aggregation process in a stochastic way by iteratively determining the probability of collision between randomly chosen ice crystals, which depends on the size and fall speed of the candidates. Due to the lack of observations, we assume random orientation and a narrow Gaussian size distribution for the ice crystals in an aggregate because of the complex flow around the snowflakes. The ice crystals are attached without overlapping to their nearest neighbor, which can make the aggregates a bit too fluffy. For the aggregates of needles, we use the method by Kajikawa et al. [2000] to attach similar-sized crystals.

In the study, we use aggregates of needles, ordinary dendrites, fern-like dendrites, and six-bullet rosettes, i.e. four out of six pristine types. Aggregates of the other types are not as common and are therefore omitted from this study. The number of crystals (or monomers) in each aggregate is varied and depends on the ice crystal type. For needles and dendrites, we use 2, 10, 20, 30, 40, and 50 monomers, while for the six-bullet rosettes, we use 2, 5, 10, 15, and 20. These values are arbitrary in the sense that natural particles can have any number of monomers, although there is a physical limit to the maximum number due to breakup. Also, the smaller number of crystals for rosette aggregates than for dendrites/needles is based on aircraft measurements [Um and McFarquhar, 2007].

Single ice crystals tend to fall in preferential orientation [Cho et al., 1981; Thomas et al., 1990; Matrosov et al., 2005; Noel and Sassen, 2005]. To simulate this, we orient the generated ice crystals according to the measurements by Noel and Sassen [2005] for warmer clouds, which indicate highly horizontal orientation with an average canting angle of about 2° and a Gaussian distribution with a standard deviation of 1°. It should be noted that these values are based on observations of planar crystals and may not be representative of all the types used in this study. The orientation of the aggregates is assumed to be random, although a recent study by Hogan et al. [2012] indicates a preferential orientation.

Examples of the modeled shapes for the different ice crystal types and their aggregates are shown in Figure c.1. Note that we only model dry pristine particles and their aggregates. We are neglecting melting, riming, and breakup, which are more poorly understood and need more in situ measurements in order to make the shape models realistic. Also, the irregularity/asymmetry of natural ice crystals is also neglected mainly due to the lack of observations.

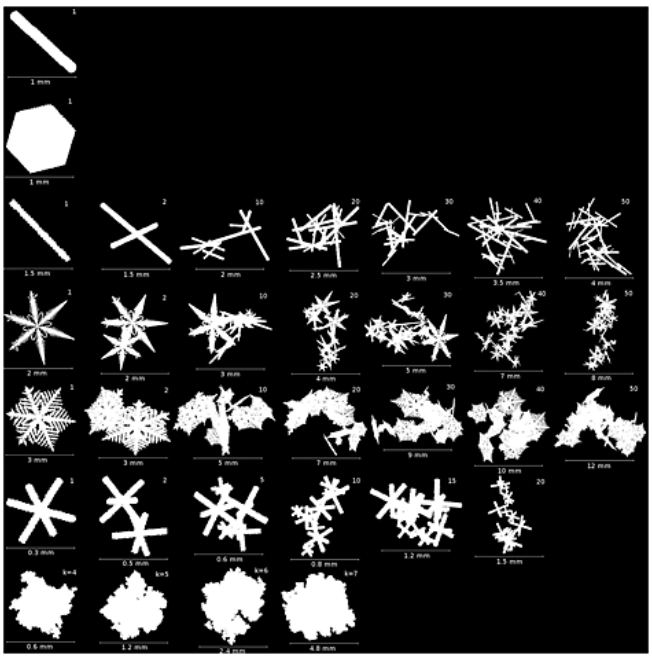

Figure c.1 Examples of the modeled snowflakes as viewed at 90° elevation angle. (top to bottom) The crystal types are hexagonal column, hexagonal plate, needle, ordinary dendrite, fern-like dendrite, six-

bullet rosette, and lump graupel. The number of crystals in an aggregate is shown on the upper right corner, while for the lump graupels, it shows the total number of iterations. The average size for each type is also shown at the bottom.

C.1.2 Physical Properties of Modeled Snowflakes

In Figure 2, we show the mass of both the modeled particles and the measured values from various field studies as a function of the maximum diameter Dmax, which can be computed in arbitrary plane: xy, xz, or yz [Korolev and Isaac, 2003]. The single ice crystals and lump graupels are shown in Figure c.2 (left), while the aggregates are in Figure c.2 (right).

The agreement between the measurements and the shape models is overall good, but some crystal types, such as the single dendrites, exhibit larger mass for the models. There are two main reasons for the differences for single crystals. First, the measured m–D relationship and the thickness-diameter ratio for ice crystals are from different studies, which can produce a selection bias. Second, the thickness-diameter ratio may not be constant over the whole crystal, as we have assumed in our 2-D dendritic

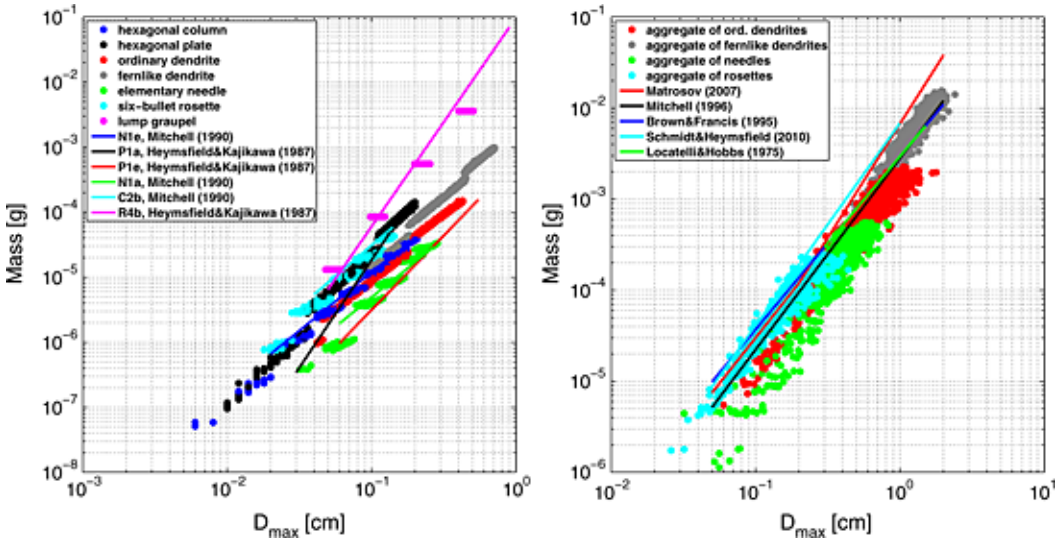

Figure c.2 (left) The mass of single ice crystals and lump graupel and (right) aggregates of ice crystals as a function of the maximum diameter. Hexagonal columns are shown in blue symbols, hexagonal plates in black, ordinary dendrites in red, fern-like dendrites in gray, needles in green, six-bullet rosettes in cyan, and lump graupels in magenta. The corresponding mass-diameter relationships from field measurements is also shown for each crystal type in Figure c.1 (left), and more general relationships for aggregates in Figure c.1 (right).

shape model. Natural dendrites accumulate more ice to the center of the branches as they grow, which produces less overall mass than our model.

For the aggregates (Figure c.2, right), the agreement between the measurements and shape models is also reasonable, although the modeled aggregates of needles and ordinary dendrites seem to have a factor of about 0.5 less mass than the measurements on average. However, it should be noted that some of the measurements include various mixtures of ice crystal types and their aggregates including both partly melted and rimed snow making a direct comparison unreliable.

The aspect ratio α is defined as the ratio between Dmax derived in some direction and the maximum diameter Dw perpendicular to this direction

$$\alpha = \frac{D_w}{D_{\max}}. \qquad \text{(c.1)}$$

In this study, we average over three perpendicular directions (xy, xz, and yz).

Figure c.3 shows the aspect ratio for the same particles. The solid lines indicate average values for each snow type. As can be seen in Figure 3 (left) for single crystals, the aspect varies between almost unity (graupel and rosettes) to about 0.06 (dendrites) with fairly large standard deviation. Gaps between clusters of data points for some particle types are due to discretization limits, since the thickness or diameter has a minimum size of one dipole. The aspect ratio for aggregates is more constrained, varying between 0.9 and 0.6 (Figure c.3, right), but does indicate slight dependence on the monomer type.

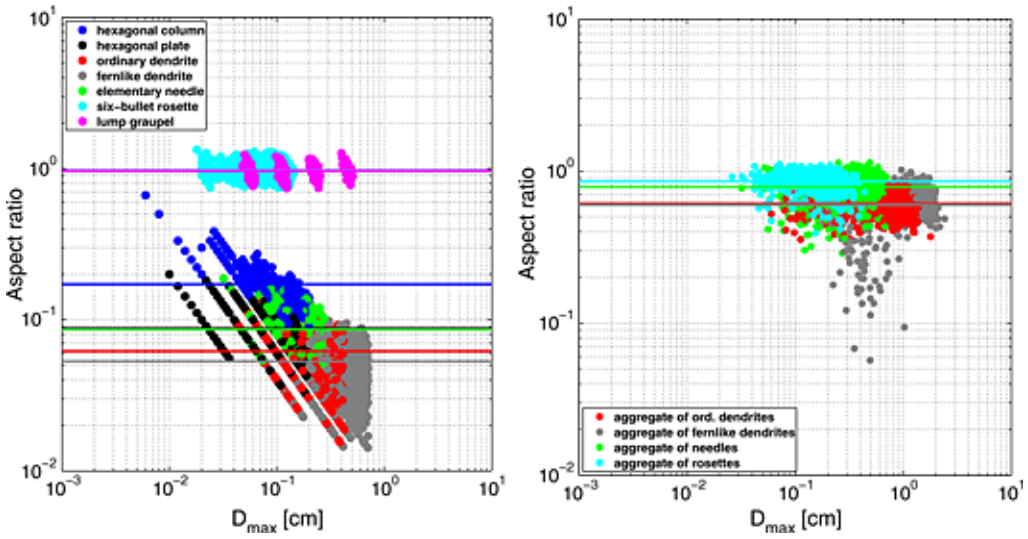

Figure c.3, Same for the figure c.2, but for the aspect ratio.

Roundness β has been used to characterize cloud ice particles by Heymsfield et al. [2002] and Korolev and Isaac [2003], modeled fractal particles by Ishimoto [2008], and modeled aggregate particles by Tyynelä et al. [2011]. In this study, we use the definition by Ishimoto [2008]:

$$\beta = \frac{4(A_{xy} + A_{xz} + A_{yz})}{3\pi D_{\max}^2}, \qquad \text{(c.2)}$$

where Axy, Axz, and Ayz are the apparent areas in three perpendicular directions. The roundness (or

area ratio) is averaged over these directions.

In Figure c.4, we show the roundness for the modeled ice crystals (left panel) and aggregates (right panel) as a function of Dmax. As can be seen, the roundness as defined in equation (2) is sensitive to the difference in ice crystal shapes varying between about 0.07 and 0.6 on average. Even aggregates produce distinct differences in roundness for different monomer types. Single ice crystals also indicate a dependence on Dmax, which is due to both the change in aspect ratio and preferential orientation.

C.1.3 Scattering Properties and Computations

To model backscattering using complex shapes, we use the discrete-dipole approximation (DDA), which is a method where the particle is divided into small volume elements (dipoles) that are placed into a regular cubic lattice [Purcell and Pennypacker, 1973]. This allows a high degree of detail in the particle shape, which can be controlled by the number of volume elements used in the shape model. The accuracy of DDA is determined both by the number of dipoles and the dipole spacing kd relative to the wavelength. Typically, it is required that $|m|kd < 0.5$, where m is the refractive index of the material. In this study, d is fixed to 20 µm for all particles, except the fern-like dendrites, which have d= 40 µm, and $|m|kd$ is 0.58 at maximum. This ensures that there are enough dipoles to approximate the shapes of

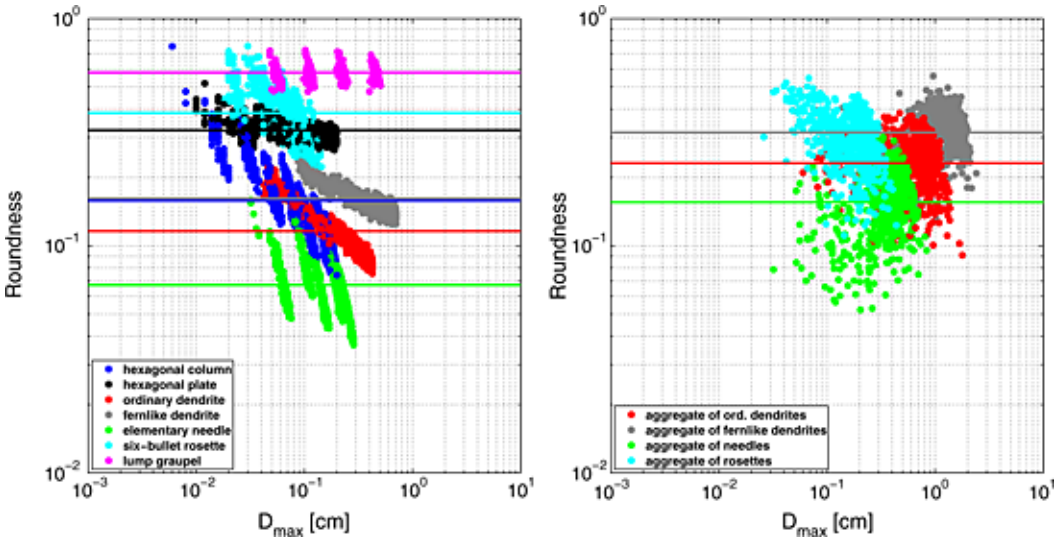

Figure c.4, Same for the figure c.2 but for the roundness.

smallest ice crystals while still keeping the memory requirements feasible for the largest particles. The refractive index of solid ice is taken from Jiang and Wu [2004]. The Amsterdam DDA program by Yurkin and Hoekstra [2011] was chosen for this study.

A volume observed by a radar is composed of many dissimilar particles in different orientations and sizes. In this paper, we are not mixing the pristine ice crystal types in a volume, since we want to show how they differ in the backscattering properties. For this purpose, we generate 1000 individual ice crystals for each type randomly chosen within the appropriate size range and 100 random aggregates of ice crystals for each type and for each number of crystals in the aggregate. For graupels, we use 100 random fractals for each number of iterations. The total number of different snowflakes used in this

study is 8700. The details of these numbers are also shown in Table 1. The radar observables are computed by numerically averaging over different size ranges depending on the snowflake type. Also, due to the preferential orientation of the ice crystals, the elevation angle of the radar is varied: 0°, 15°, 30°, 45°, 60°, 75°, and 90°.

The ADDA program produces single-particle scattering matrices, which are used together with a particle size distribution (PSD) function in computing the radar observables. We assume an exponential PSD for all the snowflakes [Matrosov, 2007; Heymsfield et al., 2008]:

$$N(D) = N_0 \exp(-\Lambda D_{\max}), \qquad \text{(c.3)}$$

where N0 is the intercept parameter and Λ the slope parameter. The median volume diameter D0 is derived from

$$\int_{D_{\text{lower}}}^{D_0} D^3 \exp(-\Lambda D)\mathrm{d}D = \frac{1}{2}\int_{D_{\text{lower}}}^{D_{\text{upper}}} D^3 \exp(-\Lambda D)\mathrm{d}D, \qquad \text{(c.4)}$$

where Dlower and Dupper are the minimum and maximum diameters for each snow type. The relationship between Λ and D0 is shown in Figure c.5.

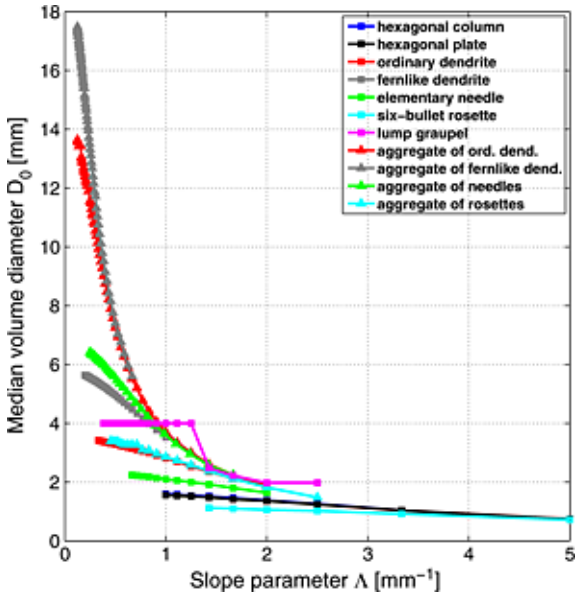

Figure c.5 The median-volume diameter D0 as a function of the slope parameter Λ for different snow types.

In Table c.1, we show Dmax and D0 ranges for each snowflake type. The Dmax ranges have been chosen to reflect the natural variation in snowflakes and are based on the values shown by Pruppacher and Klett [1997] with slightly broader ranges. The Λ values vary in steps of 0.1 mm−1 while N0 has been fixed to 104 mm−1m−3. The Λ values vary between from almost flat to highly peaked distributions. Note that we do not have DDA results for single fern-like dendrites, only their aggregates, since we wanted to balance the relative contributions from single ice crystals and aggregates to the statistical analysis.

When computing the scattering properties, we have adopted the conventions of Bohren and Huffman [1983]. The equivalent radar reflectivities (in units of mm6m−3) at different linear polarization states (hh, vv, hv, and vh) are derived from

$$Z_{\mathrm{e,\,vv/hh/hv/vh}} = \frac{8\times10^{18}}{\pi k^4 |K|^2} \int_{D_{\mathrm{lower}}}^{D_{\mathrm{upper}}} \sigma_{\mathrm{vv/hh/hv/vh}}(D) N(D) \mathrm{d}D, \tag{c.5}$$

where K = (m2−1)/(m2+2) is the dielectric factor, σvv/hh/hv/vh=4π|Svv/hh/hv/vh(180°,0°)|/k2 the backscattering cross section for linearly polarized incident wave (h and v), and Svv/hh/hv/vh are the elements of the amplitude scattering matrix. Due to reciprocity at backscattering, Ze, vh=Ze, hv leaving three independent reflectivities. These can be combined to define two radar observables: the differential reflectivity Zdr=Ze,hh/Ze,vv and the linear depolarization ratio LDRvh=Ze,vh/Ze,hh.

The linear polarization states can be transformed to circular polarization basis (l and r) by adding a phase difference of ±π/2 between the linear polarization vectors. The corresponding radar reflectivities in this case are

$$Z_{\mathrm{e,\,rr/ll/rl/lr}} = \frac{8\times10^{18}}{\pi k^4 |K|^2} \int_{D_{\mathrm{lower}}}^{D_{\mathrm{upper}}} \sigma_{\mathrm{rr/ll/rl/lr}}(D) N(D) \mathrm{d}D, \tag{c.6}$$

where σrr/ll/rl/lr=4π|Srr/ll/rl/lr(180°,0°)|/k2 is the backscattering cross sections for circularly polarized incident wave. The relationships between the linearly and circularly polarized amplitude scattering matrix elements are

$$\begin{aligned} S_{\mathrm{rr}} &= \frac{1}{2}(S_{\mathrm{vv}} + S_{\mathrm{hv}} + \mathrm{i}(S_{\mathrm{hh}} + S_{\mathrm{vh}})) \\ S_{\mathrm{ll}} &= \frac{1}{2}(S_{\mathrm{vv}} - S_{\mathrm{hv}} + \mathrm{i}(S_{\mathrm{hh}} - S_{\mathrm{vh}})) \\ S_{\mathrm{lr}} &= \frac{1}{2}(S_{\mathrm{vv}} - S_{\mathrm{hv}} - \mathrm{i}(S_{\mathrm{hh}} - S_{\mathrm{vh}})) \\ S_{\mathrm{rl}} &= \frac{1}{2}(S_{\mathrm{vv}} + S_{\mathrm{hv}} - \mathrm{i}(S_{\mathrm{hh}} + S_{\mathrm{vh}})). \end{aligned} \tag{c.7}$$

Similar to the linear polarization basis in equation (5), we can also define the circular depolarization ratio CDRrl=Ze,rr/Ze,rl.

The correlation between different polarization states of the scattered wave is defined by the correlation coefficients. A common observable for dual-polarization radars is the copolarized correlation coefficient:

$$\rho_{\mathrm{hv}} \exp(\mathrm{i}\delta_{\mathrm{hv}}) = \frac{\int_{D_{\mathrm{lower}}}^{D_{\mathrm{upper}}} S_{\mathrm{hh}}(D) S_{\mathrm{vv}}^{*}(D) N(D) \mathrm{d}D}{\sqrt{\int_{D_{\mathrm{lower}}}^{D_{\mathrm{upper}}} |S_{\mathrm{hh}}(D)|^2 N(D) \mathrm{d}D \int_{D_{\mathrm{lower}}}^{D_{\mathrm{upper}}} |S_{\mathrm{vv}}(D)|^2 N(D) \mathrm{d}D}}, \tag{c.8}$$

where ρhv is the amplitude and δhv is the argument of the correlation coefficient. δhv is also known as the backscatter differential phase and is typically expressed in degrees. As ρhv is not a strong function of shape for dry snow, we only use δhv, when analyzing the computations.

The specific differential phase is the difference between the propagation constants of h- and v-polarized waves

$$K_{\mathrm{dp}} = \frac{2\pi}{k^2} Re \int_{D_{\mathrm{lower}}}^{D_{\mathrm{upper}}} [i S_{22}(0°, 0°, D) - i S_{11}(0°, 0°, D)] N(D) \mathrm{d}D, \quad \text{(c.9)}$$

where S22(0°,0°) and S11(0°,0°) are the forward-scattered elements of the amplitude scattering matrix defined in the forward scattering alignment convention [Ulaby and Elachi, 1990]. Note that the other observables are defined in the backscattering alignment convention. Kdp is expressed in units of deg km−1.

Dual-frequency ratio (DFR) between two frequency bands (f1 and f2) is defined as

$$\mathrm{DFR}_{f_1/f_2} = \frac{Z_{\mathrm{e,hh,f_1}}}{Z_{\mathrm{e,hh,f_2}}}. \quad \text{(c.10)}$$

Note that Zdr, LDR, CDR, and DFR are independent on both the intercept parameter N0 and the dielectric factor K. Also, in this study we categorize DFRs and some polarimetric measurements as a single measurement for convenience even though they are already a combination of measurements.

C.1.4 Statistical Measures to Analyze a Data Set

Taking into account the various snowflake types used in this study, their PSD parameters, and measurement parameters, such as the elevation angle, radar frequency, and radar observables, the resulting data space becomes infeasible to analyze with simple methods. A systematic study of all possible data element combinations is difficult to present in a coherent fashion and does not reveal hidden trends and statistical significance. However, a large scattering database can be seen as a distribution in a multidimensional space and can be analyzed statistically by measuring how well clustered it is with respect to different combinations of measurement parameters. This can help in devising an optimal measurement strategy to characterize falling snow.

The goal in clustering algorithms is to use statistical measures to find a set of clusters from the data set without a priori knowledge of the optimal clustering [Halkidi et al., 2001]. In our case, the partitions, which correspond to the different snow types, are already known beforehand, so we only need to measure how clustered the partitions are. Although the measures for quantifying data clustering vary [Rendón et al., 2011], they are commonly called cluster validation indices (CVIs). Each CVI is defined in a different way and can have values ranging widely with some having a closed interval of values and some having values up to infinity. Comparing CVI values from different CVI methods can therefore be ambiguous. However, using several methods at the same time can reveal common trends and provide a more reliable basis for determining which combinations of measurement parameters are better than others in characterizing snow. Instead of comparing absolute CVI values, which can be difficult to interpret, we concentrate on the relative order for different measurements. Notice that the most promising results are those where the CVIs produce mutually similar ordering and agree with each other.

There are generally two types of CVI methods: external, which uses data from a predetermined structure to evaluate all the clusters, and internal, which uses only the data in the clusters themselves.

Since we have no preferred cluster in this study, we have chosen three common internal CVIs: the Davies-Bouldin index (DBI) [Davies, 1978], Dunn index (DI) [Dunn, 1973], and the Silhouette index (SI) [Rousseeuw, 1987].

The Davies-Bouldin index is defined as

$$\begin{aligned} A_i &= \frac{1}{N_i}\sum_{j=1}^{N_i} X_{i,j}, \\ S1_i &= \sqrt{\frac{1}{N_i}\sum_{j=1}^{N_i}(X_{i,j}-A_i)^2}, \\ M1_{ij} &= \|A_i - A_j\|, \\ \mathrm{DBI} &= \frac{1}{N_c}\sum_{i=1}^{N_c}\max_{j,j\neq i}\frac{S1_i + S1_j}{M1_{ij}}, \end{aligned} \qquad \text{(c.11)}$$

where Xi,j is the data point j in the cluster i, Ni the number of data points in the cluster i, Ai the centroid of the cluster, Nc the number of clusters, S1i within-cluster separation of the data points, M1ij the between-cluster separation for clusters i and j, and DBI the Davies-Bouldin index. DBI varies between zero and infinity. The smaller it is, the more clustered is the data set.

The Dunn index is defined as

$$\begin{aligned} S2_i &= \max_{k,l\in C_i, k\neq l}\sqrt{(X_{i,k}-X_{i,l})^2}, \\ M2_{ij} &= \min_{k\in C_i, l\in C_j}\sqrt{(X_{i,k}-X_{j,l})^2}, \\ \mathrm{DI} &= \min_{i,j,i\neq j}\frac{M2_{ij}}{\max_k S2_k}, \end{aligned} \qquad \text{(c.12)}$$

where S2i is the maximum within-cluster separation of all the data points in the cluster i, M2ij the minimum between-cluster separation for clusters i and j, and DI the Dunn index. Like DBI, DI varies between zero and infinity, but unlike DBI, a larger value indicates better clustering.
The Silhouette index is defined as

$$\begin{aligned} S3_{i,j} &= \sqrt{\frac{1}{N_i - 1}\sum_{k=1,k\neq j}^{N_i}(X_{i,j}-X_{i,k})^2}, \\ M3_{i,j} &= \min_k \sqrt{\frac{1}{N_k}\sum_{l=1}^{N_k}(X_{i,j}-X_{k,l})^2}, \\ \mathrm{Sil}_{i,j} &= \frac{M3_{i,j} - S3_{i,j}}{\max M3_{i,j}, S3_{i,j}}, \\ \mathrm{SI} &= \mathrm{avg}_{i,j}\mathrm{Sil}_{i,j}, \end{aligned} \qquad \text{(c.13)}$$

where S3i,j is the average within-cluster distance for data point j in the cluster i, M3i,j the average distance between data point j in the cluster i and the closest other cluster, Sili,j the silhouette of the data point, and SI the average Silhouette index. SI varies between −1 and 1. The closer it is to one, the more clustered the data is. Note that we use Euclidean distances and norms in all the CVIs.

In this study, the clusters represent different snow types, and the data points Xi,j different radar observable values with varying elevation angle, radar frequency, and PSD parameters (Λ and N0).

C.2 Results

In this section, we first analyze the backscattering properties statistically to reveal measurements and their combinations that can be used to characterize falling snow, then show some of these properties in more detail, and finally apply them to field measurements obtained during the GCPEx campaign.

C.2.1 Statistical Analysis of Backscattering Properties and Their Combinations

Tables c.2 and c.3 show some of the results of analyzing all of the integrated/averaged backscattering properties using the statistical measures described above. It should be noted that measurement limits and attenuation of the radar signal have not been taken into account, when computing the CVIs, which may result in unpractical characterization in some cases.

Table c.2 luster Validation for the Backscattering Properties Using the Davies-Bouldin (DBI), Dunn (DI), and Silhouette (SI) Indices

	Optimal Frequency Band			Optimal Elevation Angle (deg)		
Measurement	DBI	DI	SI	DBI	DI	SI
Z_{hh}	S (1.86)	W (7.5e−8)	W (−0.40)	45 (3.32)	75 (1.1e−7)	0 (−0.39)
Z_{dr}	Ka (0.71)	Ka (**9.2e−3**)	W (0.42)	60 (0.44)	60 (**1.0e−2**)	60 (0.33)
LDR	W (1.04)	W (4.7e−4)	Ka (0.56)	60 (0.52)	0 (4.5e−4)	90 (0.46)
CDR	W (**0.69**)	Ka (3.4e−4)	Ka (**0.68**)	0 (**0.43**)	0 (9.7e−4)	0 (**0.63**)
δ_{hv}	Ka (1.77)	W (2.7e−4)	Ka (−0.04)	90 (3.81)	0 (2.8e−4)	0 (−0.07)
K_{dp}	W (3.07)	X (4.6e−5)	W (−0.12)	90 (1.27)	30 (6.4e−5)	90 (−0.07)
$DFR_{Ku/Ka}$	-	-	-	30 (0.93)	30 (9.3e−5)	75 (0.21)
$DFR_{S/W}$	-	-	-	30 (0.85)	45 (5.0e−5)	75 (0.04)
$DFR_{Ku/W}$	-	-	-	30 (0.89)	15 (1.0e−4)	75 (0.07)
$DFR_{Ka/W}$	-	-	-	90 (1.16)	45 (1.3e−4)	75 (0.30)
$DFR_{Ka/G}$	-	-	-	90 (0.88)	0 (5.5e−4)	75 (0.58)
$DFR_{W/G}$	-	-	-	75 (1.23)	75 (4.0e−4)	75 (0.34)

a CVI values are shown in parenthesis.

Table c.3 Same as in Table 2 but for Combinations of Measurements

	Optimal Frequency Band			Optimal Elevation Angle (deg)		
Measurement Combination	DBI	DI	SI	DBI	DI	SI
$DFR_{Ku/Ka}$ + $DFR_{Ka/W}$	-	-	-	45 (0.94)	30 (1.2e−3)	90 (0.29)
$DFR_{S/Ka}$ + $DFR_{Ka/W}$	-	-	-	45 (0.90)	30 (4.7e−4)	75 (0.14)
$DFR_{S/Ku}$ + $DFR_{Ku/Ka}$	-	-	-	30 (0.93)	90 (2.0e−4)	75 (0.22)
$DFR_{Ku/Ka}$ + $DFR_{Ka/G}$	-	-	-	90 (0.71)	15 (3.6e−3)	75 (**0.48**)
$DFR_{Ku/W}$ + $DFR_{W/G}$	-	-	-	0 (0.67)	15 (1.8e−3)	90 (0.30)
$DFR_{Ka/W}$ + $DFR_{W/G}$	-	-	-	90 (0.81)	15 (7.6e−3)	75 (0.47)
$DFR_{Ku/Ka}$ + $Z_{dr,Ku}$	-	-	-	0 (**0.31**)	30 (1.3e−2)	0 (0.42)
Z_{dr} + CDR	Ka (0.32)	Ka (7.6e−2)	W (0.60)	75 (0.42)	60 (**7.1e−2**)	0 (0.44)
Z_{dr} + LDR	Ka (0.36)	Ka (6.5e−2)	W (0.54)	75 (0.42)	75 (5.2e−2)	75 (0.38)

In Table c.2, both the optimal frequency bands and elevation angles are shown for each type of measurement together with the corresponding CVI values (shown in parenthesis). For DBI, smaller values are better, while for DI and SI larger values are better. The best CVI values in each column are shown in bold font. It is clear that Zhh by itself is not as good as the other polarimetric observables for characterization, but higher frequencies seem to work better. Ka and W bands show overall best characterization for Zdr, LDR, CDR, and δhv. Slightly off-nadir elevation angles provide best results for Zdr due to the preferential orientation of the ice crystals. Both δhv and Kdp perform better than Zhh, but not as good as the other observables. There are no common trends for the elevation angles.

For DFRs, higher frequencies provide better characterization. However, 75° seems to be slightly better than nadir measurements. This may be due to the fact that at slightly off-nadir direction, the oriented ice crystals appear more asymmetrical and therefore more nonspherical, which increases the variation in σhh. Having a large difference in frequencies (S/W and Ku/W) results in worse characterization than having two higher frequencies (Ka/W, Ka/G, and W/G), although Ku/Ka combination seems to be a good pairing showing similar characterization to Ku/W.

Table c.3 shows optimal frequencies and elevation angles for combinations of measurements showed in Table c.2. As can be seen, combining measurements constrains the backscattering properties into smaller areas in the parameter space and results in better clustering/characterization overall than the results shown in Table 2. When combining two DFRs, which share one frequency, it is obvious that higher frequencies are better. Again, Ku/Ka band combination seems to be a special case showing better results than Ku/W and S/Ka combinations. For Zdr and LDR/CDR combination, Ka and W bands are optimal having better CVI values than combination of DFRs. There does not seem to be any noticeable

trend with the optimal elevation angles for DFR combinations.

At the Ku and Ka bands, combining DFR and Zdr provides a reasonable characterization at lower elevation angles due to the preferential orientation. The best overall characterization in this study is provided by combining polarimetric observables (Zdr and LDR/CDR) at the Ka and W bands.

We also checked the CVI values for the single crystals and graupel omitting the aggregates (not shown here). The overall characterization improved significantly throughout, but the relative results remained similar. Again, Zdr and CDR showed best characterization at Ka and W bands in addition to δhv. Overall, the optimal frequency bands were lower.

C.2.2 Example Combinations of Measurements

Figure c.6 shows the DFRKu/Ka and DFRKa/W combination plotted together at 0° (Figure 6, left) and 90° (Figure c.6, right) elevation angles. The results are similar to those in studies by Kneifel et al. [2011] and Leinonen et al. [2012] showing that the aggregates separate from the more spherical graupels, which have larger DFRKa/W values. This may indicate that higher-frequency measurements near nadir that produce DFRs similar to spheroidal models are due to heavily rimed snow or graupel. Note that single crystals, with the exception of rosettes, are difficult to characterize at 90° elevation (Figure 6, right) due to the preferential orientation of the crystals, which produces Rayleigh-type backscattering. However, at 0° (Figure c.6, left) they show larger separation with the dendrites and hexagonal plates clearly separating from the aggregates. On the other hand, different aggregate types are difficult to distinguish from each other.

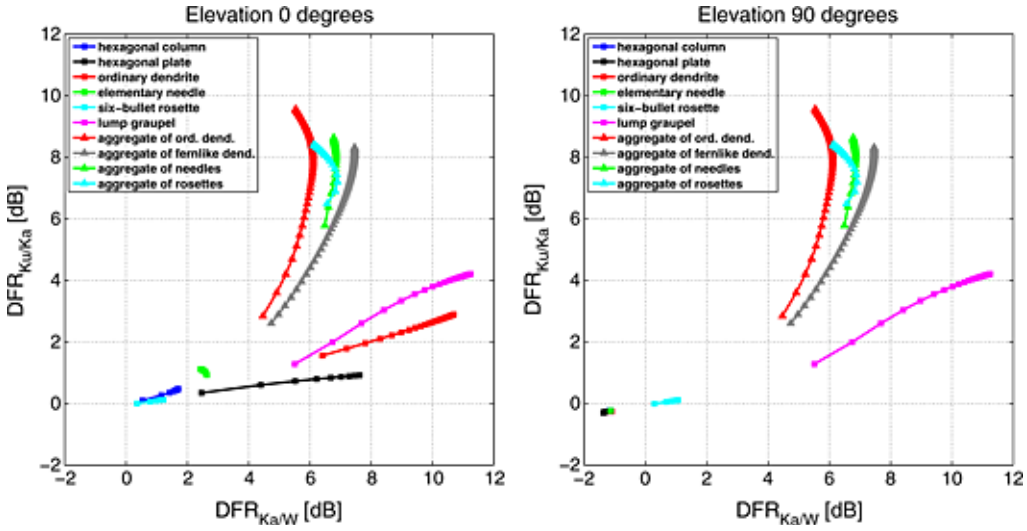

Figure c.6, The dual-frequency ratios DFRKu/Ka and DFRKa/W plotted at (left) 0° and (right) 90° elevation angles. Single crystals are shown in square symbols and aggregates in triangles with different colors representing different crystal types. Color coding is the same as in Figure c.1.

In Figure c.7, we show Zdr and CDR plotted against each other at the Ka band and at 0° (Figure c.7, left) and 60° (Figure c.7, right) elevation angles. As can be seen, at 0° this provides a fairly good characterization and produces five different clusters/snow types: hexagonal plates, dendrites, columns/needles, aggregates, and graupels/rosettes. At 60°, the clusters are closer to each other, but the variation within each cluster/snow type is smaller. This results in better overall clustering as shown

in Table c.3.

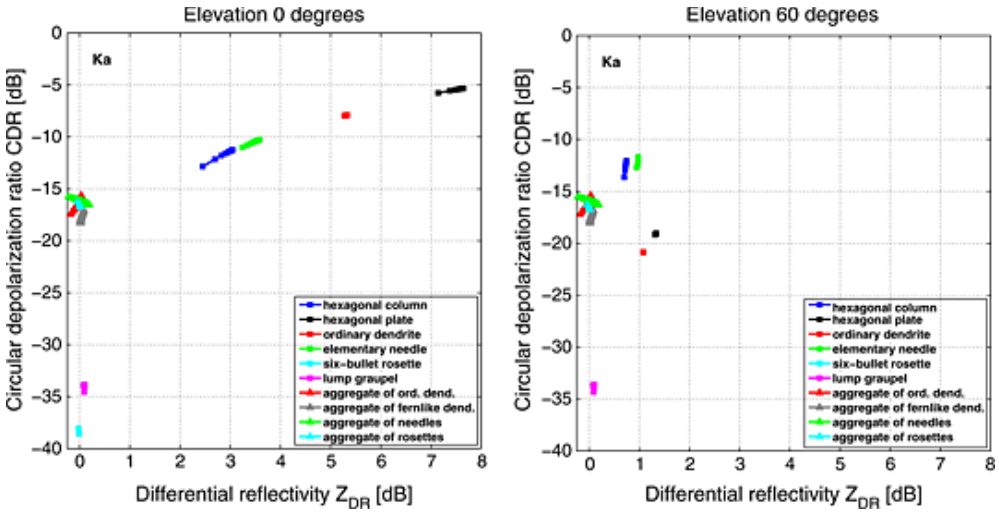

Figure c.7, The differential reflectivity Zdr and the circular depolarization ratio CDR plotted at (left) 0° and (right) 60° at the Ka band. Snow types are the same as in Figure c.6.

The relative ordering and behavior of the CDR values for different ice crystal types with respect to elevation angle is similar to the measurements shown by Reinking et al. [2002]. The only differences are the absolute levels in dB, which can be due to the different depolarization state, difference in PSD values, attenuation, etc.

C.2.3 Snowfall Case During GCPEx

The goal of the GPM Cold-season Precipitation Experiment (GCPEx) was to study how passive and active multifrequency sensors could characterize falling snow by collecting both in situ microphysical and remote sensing data. In this study, we use the measurement data from the mobile NASA D3R ground-based radar, which is a dual-polarization Doppler radar operating at Ku and Ka bands, and the APR2 radar on board the NASA DC-8 aircraft also operating at Ku and Ka bands. We also use in situ probe data from the University of North Dakota's Citation aircraft, which was flying at different altitudes during the radar measurements. For the case study, we have selected 27 January during which there was reported snowfall. During 27 January, the D3R radar was operating close to the DC-8 aircraft route and scanning within 15° in the azimuthal direction from the aircraft flight path (see Figure c.8). The APR2 radar was pointing toward the ground. The Ka data from the D3R radar could not be used in this case due to the low power of the transmitter.

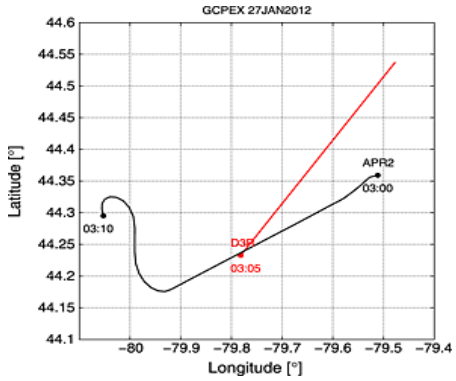

Figure c.8, Location and measurement direction of the D3R radar and the flight path of the APR2 radar.

In Figure c.9, we show Zhh at Ku band (top) and Zdr (middle) measured by the D3R radar, and DFRKu/Ka measured by the APR2 radar (bottom). As can be seen, there is a melting layer above 1 km altitude with a visible bright band (top). Between 2 and 4 km height, there are two bright (Zhh>15 dBZ) areas driven by wind shear. These areas are also associated with low Zdr values (<1 dB) and large DFRKu/Ka values (>4 dB) indicating aggregates (see Figures c.6 (right) and c.7 (left)). There are also many less bright areas (Zhh<5 dBZ) close to the aggregation areas which show larger Zdr values (>1 dB) and lower DFRKu/Ka values (<4 dB) indicating oriented ice crystals (see Figures c.6 and c.7). The Zdr values were adjusted due to an average bias of about 0.33 dB, and a local Φdp-based attenuation correction was performed for the snow volumes at the upper right part of the range-height indicators [Bringi and Chandrasekar, 2001].

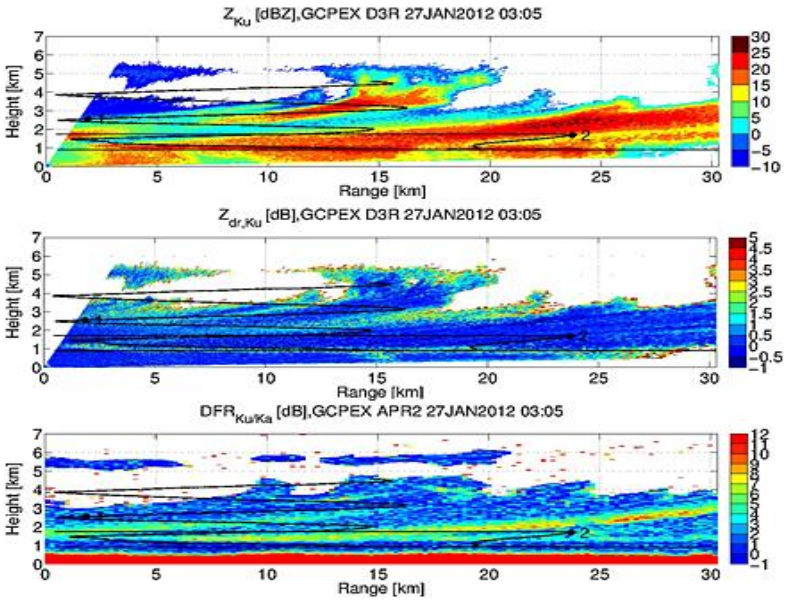

Figure c.9, (top) The equivalent reflectivity Zhh and (middle) the differential reflectivity Zdr at the Ku band measured by the D3R radar, and (bottom) the dual-frequency ratio DFRKu/Ka measured by the APR2 radar. The projected flight path of the aircraft with the particle probes is shown in the black line. Two incidents of the probe data selected for this study are shown as black dots.

For the probe data, we have selected two example cases, which indicate different particle types present in the radar volumes. The time stamp for the case 1 is 02:54 UTC and for the case 2 it is 03:19 UTC. Note that the time stamp for the radar measurements is 03:05 UTC. We show in Figure c.10 (top) an image from the Cloud Imaging Probe (CIP) as case 1, which is the site close to the D3R radar (see Figure c.9). The image reveals the presence of needle crystals and smaller irregular snow particles. When compared to Figure c.9, it is evident that these particles produce relatively low Zhh and DFR values, while also producing larger Zdr values. In Figure c.10 (bottom), we show an image from the High Volume Precipitation Spectrometer (HVPS) as case 2, which is the site further away from the D3R radar. This image reveals the presence of single needles as well as their aggregates. Again, when compared to the radar measurements in Figure c.9, they correspond to higher Zhh and DFR values, and low Zdr values.

Figure c.11 shows a scatterplot with Zdr and DFRKu/Ka plotted together using all the range-height cells in Figure c.9 with the copolarized correlation coefficient ρhv>0.9 above 2 km height. The measurements are divided into two categories: larger reflectivities (Zhh>10 dBZ) plotted as black dots and smaller reflectivities (Zhh<10 dBZ) plotted as blue dots. We also plot the results from the DDA computations with needles shown in a green area bounded by green lines, and ordinary dendrites in a red area bounded by red lines. For the computations, we have mixed the single ice crystals, their aggregates, and small irregular snow particles approximated by soft spheres in the radar volumes by varying their

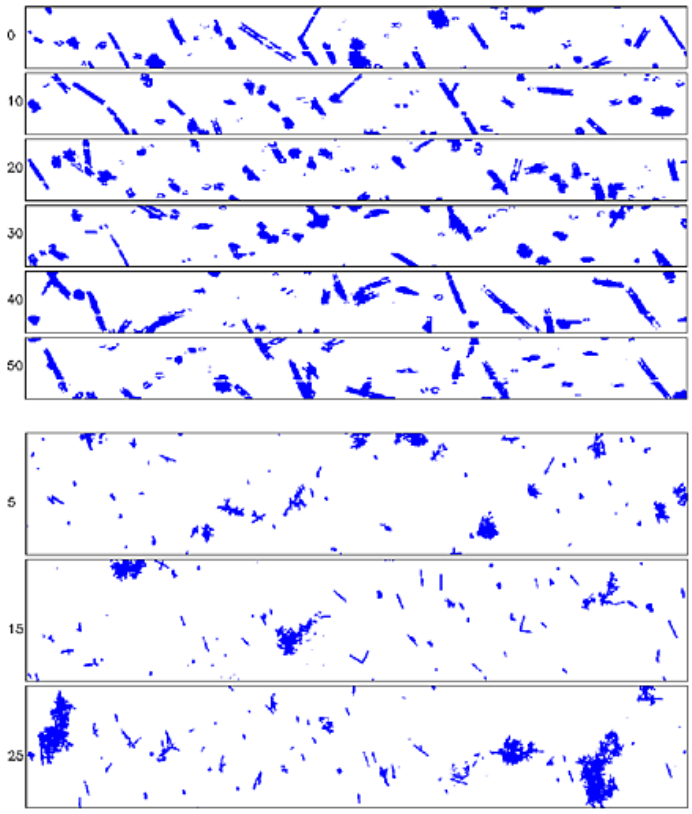

Figure c.10, Example images from the (top) Cloud Imaging Probe (CIP) and (bottom) High Volume Precipitation Spectrometer (HVPS) on board the UND

Citation aircraft. The vertical widths of the CIP and HVPS images are 1.6 mm and 19.2 mm, respectively.

relative mixing ratios between 0 and 1. We also vary D0 for all the particles as well as elevation for Zdr. For the soft spheres, we use the m–D relationship of graupels.

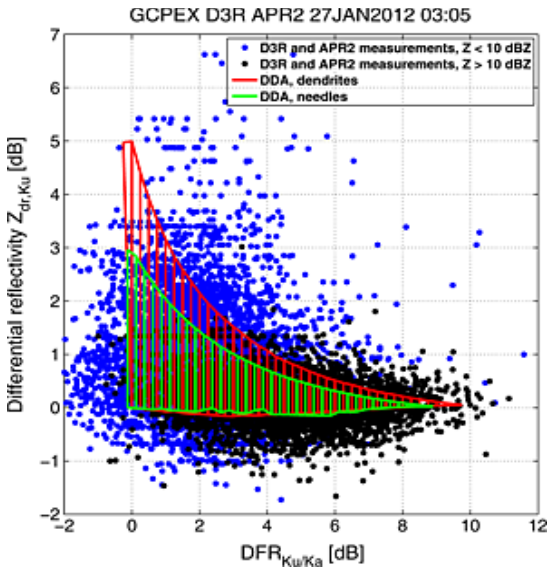

Figure c.11 The dual-frequency ratio DFRKu/Ka (X axis) and the differential reflectivity Zdr (Y axis). The radar measurements by both D3R and APR2 are shown as plus symbols. The DDA computations are shown as a green area for needles and a red area for ordinary dendrites. Note that the simulated radar volumes are a mixture of single ice crystals, their aggregates, and small irregular particles, which are approximated as soft spheres.

It is clear that in order to cover most of the measurement variation for both Zdr and DFR, three different particle models are needed. The edges of the computational areas correspond to the different particle types. Also, Zhh and DFR show strong correlation with the aggregates separating into a separate category (black dots). In order to quantify the error between the two models and the measurements, we use the CVIs presented above sections. In this case, smaller error corresponds to poorer separation/clustering between the model and the data. The CVI values for dendrites and needles are 3.0614 and 6.5659 for DBI, 3.4389e−6 and 1.5492e−5 for DI, and 0.4258 and 0.3369 for SI, respectively. Both DBI and SI indicate that needles have a smaller error than dendrites, while DI indicates the opposite. The fact that the in situ probe data show that the radar volumes contain needles and not dendrites is therefore also supported by the computational methods.

It should be noted that the large spread of the values in Figure c.11 may be due to the spatial and temporal differences between the D3R and APR2 measurements. A better volume matching will likely decrease the spread and provide a better retrieval of snow types.

C.3 Conclusion

In the present study, we have modeled physically realistic snowflakes of various shapes and sizes to

analyze their size-integrated backscattering properties. The backscattering properties have been computed at C, S, X, Ku, Ka, W, and G bands and then compared to radar observations in order to characterize snowflake types.

The results confirm that DFRs, especially at higher radar frequencies, are promising measurements to characterize snow, as already demonstrated by other studies [Kneifel et al., 2011; Leinonen et al., 2012]. They also show that, in principle, using even higher-frequency bands (G band; 220 GHz) than W can improve the characterization. However, attenuation of the radar signal may hinder its applicability. The transition region from Rayleigh scattering to the resonance region between Ku and Ka bands seems to provide overall the best characterization, while also avoiding the possible attenuation problems.

The presence of single, preferentially oriented ice crystals has a profound effect on the polarimetric backscattering properties. The results indicate that Zdr and the depolarization ratios (LDR and CDR) provide better characterization than DFRs, and this is enhanced even further by combining these measurements at the same time.

When the computations are compared to radar measurements from aircraft and ground, they show that modeling results together with dual-polarization multifrequency measurements can be used to characterize snow. They also demonstrate the advantage of combining dual-polarization measurements, especially Zdr, with dual-frequency ratios, which can narrow down characterization. Additional advantage of using these observables is that they are both independent on the intercept parameters in PSDs and therefore require less assumptions of the snowfall.

D. BAECC field experiment.

The PI participated in the field experiment phase of the ASR supported filed experiment namely BAECC. This was a unique experiment with a large number of ground instruments for in-situ snow observations and radar that actually had an influence on the future ARM program instrumentation. The participation resulted in a multi author BAMS article and the summary of the activity is as follows:

During "Biogenic Aerosols - Effects on Clouds and Climate (BAECC)", the U.S. Department Energy's Atmospheric Radiation Measurement (ARM) Program deployed the ARM 2nd Mobile Facility (AMF2) to Hyytiälä, Finland, for an 8-month intensive measurement campaign for February to September 2014. The primary research goal is to understand the role of biogenic aerosols in cloud formation. Hyytiälä is host to SMEAR-II (Station for Measuring Forest Ecosystem-Atmosphere Relations), one of the world's most comprehensive surface in-situ observation sites in a boreal forest environment. The station has been measuring atmospheric aerosols, biogenic emissions and an extensive suite of parameters relevant to atmosphere biosphere interactions continuously since 1996. Combining vertical profiles from AMF2 with surface-based in-situ SMEAR-II observations allow the processes at the surface to be directly related to processes occurring throughout the entire tropospheric column. Together with the inclusion of extensive surface precipitation measurements, and intensive observation period involving aircraft flights and novel radiosonde launches, the complementary observations provide a unique opportunity for investigating aerosol cloud interactions, and cloud-to precipitation processes, in a boreal environment. The BAECC dataset provides opportunities for evaluating and improving models of aerosol sources and transport, cloud microphysical processes, and boundary-layer structures. In addition,

numerical models are being used to bridge the gap between surface-based and tropospheric observations.

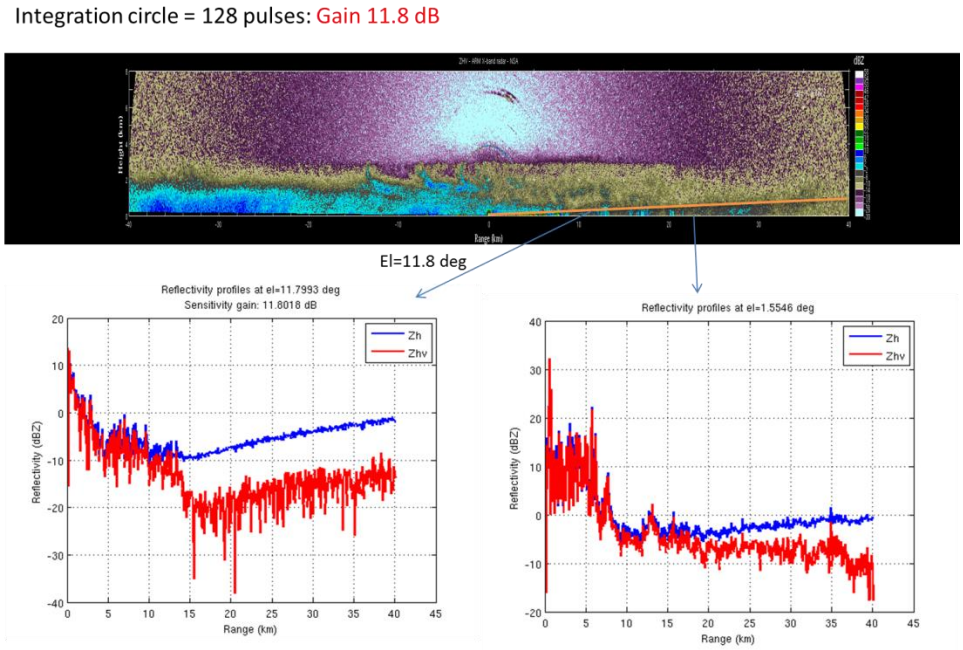

Figure D.1 Sensitivity enhancement demonstrated with the radar observations from NSA site.

REFERENCES

Atlas, D. (1954), Estimation of cloud parameters by radar, J. Meteorol., 11, 309–317.

Aydin, K., T. A. Seliga, and V. Balaji (1986), Remote sensing of hail with a dual linear polarization radar, J. Appl. Meteorol., 25, 1475–1484

Anagnostou, E. N., M. N. Anagnostou, W. F. Krajewski, A. Kruger, and B. J. Miriovsky, 2004: High-resolution rainfall estimation from X-band polarimetric radar measurements. J. Hydrometeor., 5, 110–128.

Bharadwaj, N., and V. Chandrasekar, 2011: Resolution enhancement system for networked radar system. 35th Conf. on Radar Meteorology, Pittsburgh, PA, Amer. Meteor. Soc.

Bohren, C. F., and D. R. Huffman (1983), Absorption and Scattering of Light by Small Particles, Wiley, New York.

Botta, G., K. Aydin, and J. Verlinde (2010), Modeling of microwave scattering from cloud ice crystal aggregates and melting aggregates: A new approach, IEEE Geosci. Remote Sens. Lett., 7, 572–576,

Botta, G., K. Aydin, and J. Verlinde (2013), Variability in millimeter wave scattering properties of dendritic ice crystals, J. Quant. Spectrosc. Radiat. Transfer, 131, 105–114,

Bishop, C. M., 2006: Pattern Recognition and Machine Learning. Information Science and Statistics, Springer-Verlag, 738 pp

Bringi, V. N., and V. Chandrasekar, 2001: Polarimetric Doppler Weather Radar: Principles and Applications. Cambridge University Press, 636 pp.

Bringi, V. N., G.-J. Huang, V. Chandrasekar, and E. Gorgucci, 2002: A methodology for estimating the parameters of a gamma raindrop size distribution model from polarimetric radar data: Application to a squall-line event from the TRMM/Brazil campaign. J. Atmos. Oceanic Technol., 19, 633–645.

Bringi, V. N., and V. Chandrasekar (2001), Polarimetric Doppler Weather Radar, Cambridge Univ. Press, New York.

Cho, H. R., J. V. Iribarne, and W. G. Richards (1981), On the orientation of ice crystals in a cumulonimbus cloud, J. Atmos. Sci., 38, 1111–1114.

Chandrasekar, V., and V. N. Bringi (1987), Simulation of radar reflectivity and surface measurements of rainfall, J. Atmos. Oceanic Technol., 4, 464–478.

Chandrasekar, V., and S. Lim, 2008: Retrieval reflectivity in a networked radar environment. J. Atmos. Oceanic Technol., 25, 1755–1767.

Davies, D. L. (1978), A cluster separation measure, IEEE Trans. Pattern Anal. Mach. Intell., 1, 224–227.

Dunn, J. C. (1973), A fuzzy relative of the ISODATA process and its use in detecting compact well-separated clusters, J. Cybernetics, 3, 32–57.

Gravner, J., and D. Griffeath (2009), Modeling snow crystal growth: A three-dimensional mesoscopic approach, Phys. Rev. E, 79.

Gorgucci, E., V. Chandrasekar, V. N. Bringi, and G. Scarchilli, 2002: Estimation of raindrop size distribution parameters from polarimetric radar measurements. J. Atmos. Sci., 59, 2373–2383.

Gorgucci, E., V. Chandrasekar, and L. Baldini, 2006: Correction of X-band radar observation for propagation effects based on the self-consistency principle. J. Atmos. Oceanic Technol., 23, 1668–1681.

Gorgucci, E., V. Chandrasekar, and L. Baldini, 2008: Microphysical retrievals from dual-polarization radar measurements at X band. J. Atmos. Sci., 25, 729–741.

Halkidi, M., Y. Batistakis, and M. Vazirgiannis (2001), On clustering validation techniques, J. Intell. Inf. Syst., 17, 107–145.

Heymsfield, A. J., and M. Kajikawa (1987), An improved approach to calculating terminal velocities of plate-like crystals and graupel, J. Atmos. Sci., 44, 1088–1099.

Heymsfield, A. J., S. Lewis, A. Bansemer, J. Iaquinta, L. M. Miloshevich, M. Kajikawa, C. Twohy, and M. R. Poellot (2002), A general approach for deriving the properties of cirrus and stratiform ice cloud particles, J. Atmos. Sci., 59, 3–29.

Heymsfield, A. J., P. R. Field, and A. Bansemer (2008), Exponential size distributions for snow, J. Atmos. Sci., 65, 4017–4031.

Hogan, R. J., L. Tian, P. R. A. Brown, C. D. Westbrook, A. J. Heymsfield, and J. D. Eastment (2012), Radar scattering from ice aggregates using the horizontally aligned oblate spheroid approximation, J. Appl. Meteorol. Clim., 51, 655–671.

Ishimoto, H. (2008), Radar backscattering computations for fractal-shaped snowflakes, J. Meteor. Soc. Jpn., 86, 459–469.

Jiang, J. H., and D. L. Wu (2004), Ice and water permittivities for millimeter and sub-millimeter remote sensing applications, Atmos. Sci. Lett., 5, 146–151.

Junyent, F., and V. Chandrasekar, 2009: Theory and characterization of weather radar networks. J. Atmos. Oceanic Technol., 26, 474–491.

Junyent, F., V. Chandrasekar, D. McLaughlin, E. Insanic, and N. Bharadwaj, 2010: The CASA Integrated Project 1 networked radar system. J. Atmos. Oceanic Technol., 27, 61–78.

Kalogiros, J., M. N. Anagnostou, E. N. Anagnostou, M. Montopoli, E. Picciotti, and F. S. Marzano, 2013: Optimum estimation of rain microphysical parameters from X-band dual-polarization radar observables. IEEE Trans. Geosci. Remote Sens., 51, 3063–3076.

Kajikawa, M., K. Kikuchi, Y. Asuma, Y. Inoue, and N. Sato (2000), Aggregation of needle snow crystals, Atmos. Res., 55, 131–138.

Kneifel, S., M. Kulie, and R. Bennartz (2011), A triple frequency approach to retrieve microphysical snowfall parameters, J. Geophys. Res., 116.

Korolev, A., and I. G. Isaac (2003), Roundness and aspect ratio of particles in ice clouds, J. Atmos. Sci., 60, 1795–1808.

Leinonen, J., S. Kneifel, D. Moisseev, J. Tyynelä, S. Tanelli, and T. Nousiainen (2012), Evidence of nonspheroidal behavior in millimeter-wavelength radar observations of snowfall, J. Geophys. Res., 117.

Libbrecht, K. G. (2005), The physics of snow crystals, Rep. Prog. Phys., 68, 855–895.

Lim, S., V. Chandrasekar, P. Lee, and A. P. Jayasumana, 2011: Real-time implementation of a network-based attenuation correction in the CASA IP1 testbed. J. Atmos. Oceanic Technol., 28, 197-209.

Magono, C., and C. W. Lee (1966), Meteorological classification of natural snow crystals, J. Fac. Sci., Hokkaido Univ., Ser. VII, 2(4), 321–362.

Matrosov, S. Y. (2007), Modeling backscatter properties of snowfall at millimeter wavelengths, J. Atmos. Sci., 64, 1727–1736.

Matrosov, S. Y. (1998), A dual-wavelength radar method to measure snowfall rate, J. Appl. Meteorol., 37, 1510–1521.

Matrosov, S. Y., A. J. Heymsfield, and Z. Wang (2005), Dual-frequency radar ratio of nonspherical atmospheric hydrometeors, J. Geophys. Res., 32.

Marshall, J. S., and W. McK. Palmer, 1948: The distribution of raindrops with size. J. Meteor., 5, 165–166, doi:10.1175/1520-0469(1948)005<0165:TDORWS>2.0.CO;2.

Mega, T., K. Monden, T. Ushio, K. Okamoto, Z. Kawasaki, and T. Morimoto, 2007: A low-power high-resolution broadband radar using a pulse compression technique for meteorological application. IEEE Geosci. Remote Sens. Lett., 4, 392–396.

Meneghini, R., T. Kozu, H. Kumagai, and W. C. Boncyk (1992), A study of rain estimation methods from space using dual-wavelength radar measurements at near-nadir incidence over ocean, J. Atmos. Oceanic Technol., 9, 364–382.

Moisseev, D. N., and V. Chandrasekar, 2007: Examination of the μ–Λ relation suggested for drop size distribution parameters. J. Atmos. Oceanic Technol., 24, 847–855.

Nakaya, U. (1954), Snow Crystals: Natural and Artificial, Harvard Univ. Press, Cambridge.

Nocedal, J., and S. Wright, 1999: Numerical Optimization. Springer.

Nowell, H., G. Liu, and R. Honeyager (2013), Modeling the microwave single-scattering properties of aggregate snowflakes, J. Geophys. Res. Atmos., 118, 7873–7885.

Petty, G. W., and W. Huang (2010), Microwave backscatter and extinction by soft ice spheres and complex snow aggregates, J. Atmos. Sci., 67, 769–787.

Purcell, E. M., and C. R. Pennypacker (1973), Scattering and absorption of light by non-spherical dielectric grains, Astrophys. J., 186, 705–714.

Picciotti, E., and Coauthors, 2013: Coupling X-band dual-polarized mini-radars and hydro-meteorological forecast models: The HYDRORAD project. Nat. Hazards Earth Syst. Sci., 13, 1229–1241.

Pruppacher, H. R., and J. D. Klett (1997), Microphysics of Clouds and Precipitation, chap. 2, 51 pp., Dordrecht, Boston.

Reinking, R. F., S. Y. Matrosov, R. A. Kropfli, and B. W. Bartram (2002), Evaluation of a 45° slant quasi-linear radar polarization state for distinguishing drizzle droplets, pristine ice crystals, and less regular ice particles, J. Atmos. Oceanic Technol., 19, 296–321.

Reiter, C. A. (2005), A local cellular model for snow crystal growth, Chaos, Solitons Fractals, 23, 1111–1119.

Rendón, E., I. Abundez, A. Arizmendi, and E. M. Quiroz (2011), Internal versus External cluster validation indexes, Int. J. Comp. Commun., 5, 27–34.

Rousseeuw, P. J. (1987), Silhouettes: A graphical aid to the interpretation and validation of cluster analysis, J. Comput. Appl. Math., 20, 53–65.

Seliga, T. A., and V. N. Bringi (1976), Potential use of radar differential reflectivity measurements at orthogonal polarizations for measuring precipitation, J. Appl. Meteorol., 15, 69–76.

Straka, J. M., D. S. Zrnić, and A. V. Ryzhkov (2000), Bulk hydrometeor classification and quantification using polarimetric radar data: Synthesis of relations, J. Appl. Meteorol., 39, 1341–1372.

Thomas, L., J. C. Cartwright, and D. P. Wareing (1990), Lidar observations of the horizontal orientation of ice crystals in cirrus clouds, Tellus B, 42, 211–216.

Tyynelä, J., J. Leinonen, D. Moisseev, and T. Nousiainen (2011), Radar backscattering from snowflakes: Comparison of fractal, aggregate and soft-spheroid models, J. Atmos. Oceanic Technol., 28, 1365–1372.

Ulaby, F. T., and C. Elachi (1990), Radar Polarimetry for Geoscience Applications, Artech House, Norwood.

Um, J., and G. M. McFarquhar (2007), Single-scattering properties of aggregates of bullet rosettes in cirrus, J. Appl. Meteor. Clim., 46, 757–775.

Westbrook, C. D., R. C. Ball, and P. R. Field (2006), Radar scattering by aggregate snowflakes, Q. J. R. Meteorol. Soc., 128, 1–17.

Westbrook, C. D. (2004), Universality in snow formation, PhD thesis, Univ. of Warwick, Coventry, U. K.

Yoshikawa, E., T. Ushio, Z. Kawasaki, and V. Chandrasekar, 2012: Dual-directional radar observation for preliminary assessment of the Ku-band broadband radar network. J. Atmos. Oceanic Technol., 29, 1757–1768.

Yoshikawa, E., V. Chandrasekar, and T. Ushio, 2014: Raindrop size distribution (DSD) retrieval for X-band

dual-polarization radar. J. Atmos. Oceanic Technol., 31, 387–403.

Yurkin, M. A., and A. G. Hoekstra (2011), The discrete-dipole-approximation code ADDA: Capabilities and known limitations, J. Quant. Spectrosc. Radiat. Transfer, 112, 2234–2247.